

REPORT DOCUMENTATION PAGE

Form Approved
OMB No. 0704-0188

The public reporting burden for this collection of information is estimated to average 1 hour per response, including the time for reviewing instructions, searching existing data sources, gathering and maintaining the data needed, and completing and reviewing the collection of information. Send comments regarding this burden estimate or any other aspect of this collection of information, including suggestions for reducing the burden, to the Department of Defense, Executive Service Directorate (0704-0188). Respondents should be aware that notwithstanding any other provision of law, no person shall be subject to any penalty for failing to comply with a collection of information if it does not display a currently valid OMB control number.

PLEASE DO NOT RETURN YOUR FORM TO THE ABOVE ORGANIZATION.

1. REPORT DATE (DD-MM-YYYY) 07-06-2012	2. REPORT TYPE Final Report	3. DATES COVERED (From - To) Jun 2009 - Nov 2011
---	--------------------------------	---

4. TITLE AND SUBTITLE Location and Navigation with Ultra-Wideband Signals	5a. CONTRACT NUMBER
	5b. GRANT NUMBER FA9550-09-1-0269
	5c. PROGRAM ELEMENT NUMBER

6. AUTHOR(S) Liuqing Yang, John Harris	5d. PROJECT NUMBER
	5e. TASK NUMBER
	5f. WORK UNIT NUMBER

7. PERFORMING ORGANIZATION NAME(S) AND ADDRESS(ES) University of Florida Office of Engineering Research 339 Weil Hall Gainesville, FL 32611-0000	8. PERFORMING ORGANIZATION REPORT NUMBER
--	--

9. SPONSORING/MONITORING AGENCY NAME(S) AND ADDRESS(ES) AF Office of Scientific Research 875 N. Randolph St. Room 3112 Arlington, VA 22203	10. SPONSOR/MONITOR'S ACRONYM(S) AFOSR
	11. SPONSOR/MONITOR'S REPORT NUMBER(S) AFRL-OSR-VA-TR-2012-0931

12. DISTRIBUTION/AVAILABILITY STATEMENT
Approved for Public Release; distribution is Unlimited.

13. SUPPLEMENTARY NOTES

14. ABSTRACT
Existing positioning and navigation applications mainly rely on GNSS. However, its application to indoor, metropolitan and heavy-foliage scenarios is significantly constrained by the satellite visibility, limited accuracy and the intensively frequency-selective channel condition. In this research, we investigated ranging and localization techniques using ultra-wideband (UWB) signals. In particular, we have developed two time-of-arrival (ToA) estimators for single-band UWB signals. To generalize them to multi-band UWB signals, we investigated the pros and cons of coherent and non-coherent multi-band signal combining, and studied the phase rotation calibration in order to facilitate effective coherent combining. Last but not least, we developed cooperative localization algorithms based on semi-definite programming (SDP) and developed algorithms based on semi-definite programming (SDP) and developed algorithms exploiting Doppler shift in mobile scenarios. On these subjects, we have published/submitted 13 peer-reviewed journal and conference papers.

15. SUBJECT TERMS
ultra-wideband, positioning, localization

16. SECURITY CLASSIFICATION OF:			17. LIMITATION OF ABSTRACT	18. NUMBER OF PAGES	19a. NAME OF RESPONSIBLE PERSON
a. REPORT U	b. ABSTRACT U	c. THIS PAGE U	UU	68	Liuqing Yang 19b. TELEPHONE NUMBER (Include area code) (970) 491-6215

Final Report

**LOCATION AND NAVIGATION
WITH ULTRA-WIDEBAND SIGNALS**

Liuqing Yang
(Technical Point of Contact)
Dept. of Electrical and Computer Engineering
1373 Campus Delivery
Colorado State University
Fort Collins, CO 80523
Tel: (970) 491-6215
Fax: (970) 491-2249
Email: lqyang@engr.colostate.edu

Ms. Roslyn S. Oleson
(Administrative Point of Contact)
Office of Engineering Research
College of Engineering
P.O. Box 116550
University of Florida
Gainesville, FL 32611-6550
Tel: (352) 392-9447 ext. 7
Fax: (352) 846-1471
Email: roleson@ufl.edu

Contents

A Abstract	1
B Overview	1
C Ranging with Single-Band UWB Signals: A Maximum-Likelihood Approach	3
C.1 Signal Model	3
C.2 ML Timing Algorithm and Its Acquisition Performance	5
C.2.1 ML Timing Algorithm	5
C.2.2 Acquisition Performance of the ML timing Algorithm	7
C.3 Training Sequence Design and The SML Algorithm	9
C.3.1 The Optimum Training Sequence Pattern	9
C.3.2 Simplified ML (SML) Algorithm	10
C.4 Implementation Considerations and Simulated Performance	12
C.5 Summary	14
D Ranging with Single-Band UWB Signals: Focusing-on-First-arrival (FoFa)	15
D.1 Broadband System Model with FDE	16
D.2 Energy Leakage in Channel Estimate	18
D.3 The Proposed ToA Estimator	20
D.3.1 Analysis of ToA Estimation Criterion	21
D.3.2 ToA Estimation for Multipath Channels	24
D.3.3 FoFa versus Traditional ToA Estimators	25
D.4 Summary	26
E Ranging with Multi-Band UWB Signals: Coherent vs. Noncoherent Combination	26
F Ranging with Multi-Band UWB Signals: Random Phase Rotation	29
F.1 MB-OFDM System Model	30
F.2 Channel Estimation with Coherent Combining	32
F.3 Analysis and Calibration of Random Phase Rotation Effect	33
F.3.1 With Random Phase Rotations	34
F.3.2 Without Random Phase Rotations	35
F.3.3 Phase Rotation Calibration Algorithm	36

F.3.4	Discussions	37
F.4	Simulations	37
F.5	Summary	38
G	From Ranging to Localization: Cooperative Localization via SDP	38
G.1	Cooperative Localization Algorithms	40
G.1.1	ToA	40
G.1.2	RSS	42
G.2	Cramér-Rao Lower Bound	43
G.2.1	ToA	43
G.2.2	RSS	44
G.2.3	Cooperative vs. Non-cooperative Localization	45
G.3	Effects of Semidefinite Cones	46
G.3.1	Types of Semidefinite Cones	46
G.3.2	Performance comparisons	47
G.3.3	Complexity comparisons	48
G.4	Simulations	49
G.5	Summary	50
H	From Ranging to Localization: Exploiting Doppler Effects	51
H.1	System Description	52
H.1.1	Straightforward Approach	53
H.2	Case I: Known v , Known θ	54
H.2.1	The Basic Algorithm	55
H.2.2	Ambiguity Issues	55
H.2.3	Algorithm Flowchart	57
H.2.4	Simulations	57
H.3	Case II: Known v , Unknown θ	59
H.3.1	The Basic Algorithm	60
H.3.2	Ambiguity Issues	61
H.3.3	Algorithm Flowchart	62
H.3.4	Simulations	62
H.4	Summary	62

A Abstract

Existing positioning and navigation applications mainly rely on GNSS. However, its application to indoor, metropolitan and heavy-foliage scenarios is significantly constrained by the satellite visibility, limited accuracy and the intensively frequency-selective channel condition. In this research, we investigated ranging and localization techniques using ultra-wideband (UWB) signals. In particular, we have developed two time-of-arrival (ToA) estimators for single-band UWB signals. To generalize them to multi-band UWB signals, we investigated the pros and cons of coherent and non-coherent multi-band signal combining, and studied the phase rotation calibration in order to facilitate effective coherent combining. Last but not least, we developed cooperative localization algorithms based on semi-definite programming (SDP) and developed algorithms exploiting Doppler shift in mobile scenarios. On these subjects, we have published/submitted 13 peer-reviewed journal and conference papers [1-13].

B Overview

The proposed research aims at the fundamental understanding and system-level development of alternative location and navigation in GPS-denied scenarios such as indoor, metropolitan and heavy-foliage environments, where the application of GPS is significantly constrained by the satellite visibility, limited accuracy and the intensively frequency-selective channel condition. When GPS is also available, techniques developed here can be used to enhance the GPS precision.

For time-of-arrival (ToA) based geo-location, the precision of ToA estimate is crucial. The latter, however, is challenging in environments with extensive, and often unknown, multipath, such as heavy foliage, indoor or inside caves. Traditionally, this problem is treated as a channel estimation problem, where the ToA is obtained as a by-product. However, such an approach not only induces significant complexity especially in extensive multipath, but also leads to unnecessary ToA errors as the optimality criterion for a channel estimator accounts for timing, amplitude and phase errors of all taps. To this end, we developed estimators focusing on the ToA estimation, and without any direct channel estimation. Results show that significant complexity reduction and accuracy improvement can be achieved when compared to the current state-of-the-art.

For multi-band orthogonal frequency-division multiplexing (MB-OFDM) ultrawide-band (UWB) systems, we estimated the ToA of wireless channels by using the widely adopted equally-spaced channel estimator. By suppressing the energy leakage due to the imperfect sampling of the leading channel paths, we proposed a novel ToA estimator for the MB-OFDM UWB system. This ToA estimator is evaluated and compared with the space alternating generalized expectation maximization (SAGE) algorithm. Simulation results show that the proposed ToA estimator performs well in all channel models and outperforms SAGE by directly locating the first channel path.

We further investigated the random phase rotation problem for MB-OFDM UWB systems. Random phase rotations need to be calibrated for coherent combining of MB channel information for high resolution time-of-arrival estimation. Our analysis indicates that in the presence of random phase rotations, energy leakage in the estimated channel increases and hence the ToA resolution of MB-OFDM signals degrades. Based on this, we propose to calibrate random phase rotations across subbands by minimizing energy leakage. Simulation results show that the proposed technique performs well in 802.15.4a UWB channels.

When it comes to range measurement data fusion into positioning and location estimate, we considered cooperative localization by introducing and generalizing the application of semidefinite programming (SDP). The SDP approach has been widely used to convert non-convex problems into convex ones in recent years. In our work, we apply the SDP approach to cooperative localization where the inter-target communication capability is exploited for the purpose of coverage extension and accuracy enhancement. Cooperative ToA and Received Signal Strength (RSS) minimax SDP algorithms are also proposed. Simulations show that the cooperative localization with SDP can achieve satisfying performance with considerably reduced complexity. In addition, we propose a virtual anchor concept to further improve the localization accuracy, especially in the outside-of-the-convex-hull situations.

Among the various positioning techniques, the angle-of-arrival (AoA) has traditionally been realized with large and costly antenna arrays. On the other hand, motion of the mobile target will induce Doppler which is determined by the AoA of the incoming signal. Exploiting this Doppler, we developed Doppler-aided AoA estimators for mobile targets. By studying the geometrical relationship among the target and anchors, we successfully linearized the nonlinear problem, resulting in a low-complexity solution. We have also proved the uniqueness of the solution using geometric tools. Interestingly, though the problem is formulated as AoA-based geo-location (since the Doppler can only indicate the direction of

the target), the solution is obtained via a ToA-alike technique as the position of the target is found to be the unique intersection of three circles (trilateration) each determined by two anchors.

C Ranging with Single-Band UWB Signals: A Maximum-Likelihood Approach

UWB technology exhibits prominent features in many wireless communications, networking and localization applications. Since the ultrashort pulse waveform is transmitted at very low power in UWB systems, accurate and rapid timing estimation becomes one of the most critical challenges.

In this research, we address this issue via the establishment of a data-aided maximum likelihood (ML) timing algorithm. Based on the ML criterion, estimation of all multipath gains and delays was pursued in some existing work in the literature. However, they often assume an unrealistic multipath channel model with no inter-path overlapping. The real channel with a large number of dense taps would make this method impossible to implement. Here, we focus on estimation of a single parameter, namely, the delay of the first arriving path, without invoking any unrealistic channel model assumption. We will show that our ML estimator is able to collect multipath energy, although it does not explicitly involve multipath channel estimation.

Considering the ML acquisition performance and the consistency requirement, we obtain the *unique* optimum training pattern with which the ML algorithm can be simplified, thus giving rise to the simplified ML (SML).

Fine timing with high accuracy is critical to localization with UWB technology. While the data-aided SML estimator can theoretically achieve any resolution level, they may suffer from the ambiguity induced by the weak tail of the multipath channel and the extent of the noise-only region between consecutive symbols. To circumvent the ambiguity, we supplement the SML algorithm with one more step to search for the peak of the first-order difference of the objective functions. By doing so, chip-level fine timing can be achieved.

C.1 Signal Model

In impulse-radio UWB systems, every information symbol is transmitted over a duration of T_s consisting of N_f frames. During each frame of T_f seconds, a data-modulated ultra-short pulse $p(t)$ with duration $T_p \ll T_f$ is transmitted. With binary pulse amplitude modulation (PAM), the training symbols are drawn from the binary alphabet $\{\pm 1\}$, and the transmitted waveform for a single user is modeled as:

$$v(t) = \sqrt{\mathcal{E}} \sum_{n=0}^{+\infty} s_n p_T(t - nT_s), \quad (1)$$

where \mathcal{E} is the energy per pulse and $p_T(t) = \sum_{j=0}^{N_f-1} p(t - jT_f - c_j T_c)$ represents the *symbol-long transmitted* waveform composed of N_f pulses. The pulse during the j th frame is shifted by the time-hopping code c_j , which takes integer value in the range of $[0, N_c - 1]$. The chip duration is $T_c = T_f/N_c$.

After propagating through a multipath channel with L_c taps, the received waveform can be written as $r(t) = \sum_{l=0}^{L_c-1} \alpha_l v(t - \tau_l) + \eta(t)$, where α_l and τ_l denote the attenuation and delay of the l th channel tap, and $\eta(t)$ is the zero-mean additive white Gaussian noise (AWGN) with power spectral density (PSD) $N_0/2$. The channel is assumed to be either deterministic or quasi-static over one transmission burst. We decouple the propagation delay τ_0 from the dispersive effects of the multipath channel by defining a set of relative delays with respect to τ_0 , namely $\tau_{l|0} \triangleq \tau_l - \tau_0, \forall l$. Without loss of generality (WLOG), $\tau_0 \in [0, T_s)$ is assumed in this work. Then the *symbol-long received* waveform capturing the multipath channel effects is given by:

$$p_R(t) = \sum_{l=0}^{L_c-1} \alpha_l p_T(t - \tau_{l|0}), \quad (2)$$

and the received waveform can be rewritten as:

$$r(t) = \sqrt{\mathcal{E}} \sum_{n=0}^{+\infty} s_n p_R(t - nT_s - \tau_0) + \eta(t). \quad (3)$$

To develop the ML timing algorithm, we assume that ISI is absent, but inter-frame interference may be present. This condition can be easily satisfied by constraining the last frame of each symbol such that the nonzero support of $p_R(t)$ does not extend beyond the range $[0, T_s)$. Note that this setup can also accommodate high-rate transmissions since the inter-frame interference is allowed.

For convenient manipulation, we divide the received signal into K consecutive symbol-long segments and shift them so that they all lie in the range $t \in [0, T_s)$: $r_k(t) \triangleq r(t + kT_s)\text{rect}(t)$, $k = 1, \dots, K$, where $\text{rect}(t) = 1$, $t \in [0, T_s)$, is the *window* function. Substituting (3) and defining $\eta_k(t) \triangleq \eta(t + kT_s)\text{rect}(t)$, we have the received segments:

$$r_k(t) = \sqrt{\mathcal{E}} \sum_{n=0}^{+\infty} s_n p_R(t + kT_s - nT_s - \tau_0)\text{rect}(t) + \eta_k(t), \quad \forall k. \quad (4)$$

Since $p_R(t)$ and $\text{rect}(t)$ are confined within a finite support $[0, T_s)$, it can be easily induced that for a certain segment k only $n = k - 1$ and $n = k$ contribute nonzero summands to $r_k(t)$, and (4) can be explicitly expressed as $r_k(t) = \sqrt{\mathcal{E}} (s_{k-1} p_R(t + T_s - \tau_0) + s_k p_R(t - \tau_0)) \text{rect}(t) + \eta_k(t)$, $\forall k$.

Stack the total K received segments into a vector, and define $\mathbf{r}(t) \triangleq [r_1(t), \dots, r_K(t)]^T$, $\mathbf{s}_1 \triangleq [s_0, \dots, s_{K-1}]^T$, $\mathbf{s}_2 \triangleq [s_1, \dots, s_K]^T$ and $\boldsymbol{\eta}(t) \triangleq [\eta_1(t), \dots, \eta_K(t)]^T$. Then the signal model can be rewritten in the following compact vector form:

$$\mathbf{r}(t) = \sqrt{\mathcal{E}} \mathbf{s}_1 p_R^{(a)}(t; \tau_0) + \sqrt{\mathcal{E}} \mathbf{s}_2 p_R^{(b)}(t; \tau_0) + \boldsymbol{\eta}(t), \quad (5)$$

where $p_R^{(a)}(t; \tau_0) \triangleq p_R(t + T_s - \tau_0)\text{rect}(t)$ and $p_R^{(b)}(t; \tau_0) \triangleq p_R(t - \tau_0)\text{rect}(t)$ consist of the circularly shifted version of the symbol-long received waveform $p_R(t)$. It is noteworthy that $p_R^{(a)}(t; \tau_0)$ and $p_R^{(b)}(t; \tau_0)$ are not overlapping in time; that is, the former is strictly zero for $t \in [\tau_0, T_s)$, and the latter is strictly zero for $t \in [0, \tau_0)$.

C.2 ML Timing Algorithm and Its Acquisition Performance

In this section, we will first develop the ML timing algorithm for arbitrary known transmitted symbol sequences, and then evaluate the timing acquisition performance of the algorithm.

C.2.1 ML Timing Algorithm

With the signal model in (5), the deterministic but unknown parameters are: i) the overall received symbol-long waveform $p_R(t)$ (or equivalently, its circularly shifted version $p_R^{(a)}(t; \tau_0)$ and $p_R^{(b)}(t; \tau_0)$) which carries the dispersive multipath channel information; and ii) the propagation delay τ_0 . Given $p_R(t)$ and τ_0 , the log-likelihood function for (5) bears the form:

$$\ln \Lambda(\mathbf{r}(t); p_R(t), \tau_0) \propto \int_0^{T_s} -\|\mathbf{r}(t) - \sqrt{\mathcal{E}} \mathbf{s}_1 p_R^{(a)}(t; \tau_0) - \sqrt{\mathcal{E}} \mathbf{s}_2 p_R^{(b)}(t; \tau_0)\|^2 dt$$

$$\propto \int_0^{T_s} 2\sqrt{\mathcal{E}} \mathbf{r}^T(t) \left(\mathbf{s}_1 p_R^{(a)}(t; \tau_0) + \mathbf{s}_2 p_R^{(b)}(t; \tau_0) \right) - \mathcal{E} \left\| \mathbf{s}_1 p_R^{(a)}(t; \tau_0) + \mathbf{s}_2 p_R^{(b)}(t; \tau_0) \right\|^2 dt. \quad (6)$$

Our task is to obtain the ML estimates for $p_R(t)$ and τ_0 by maximizing (6). We use the notation \tilde{x} to indicate a conjecture of unknown parameter x . The ML estimation will be accomplished in two stages: based on a fixed conjecture $\tilde{\tau}_0$, we first obtain $\hat{p}_R(t; \tilde{\tau}_0)$ as a function of $\tilde{\tau}_0$; then we replace $p_R(t)$ with $\hat{p}_R(t; \tilde{\tau}_0)$ in (6) to find the ML estimate of $\hat{\tau}_0$.

In the first stage, the integral can be removed without affecting the optimality, since the ML estimate of $p_R(t)$ is to be obtained in an instantaneous manner. As emphasized before, given a candidate $\tilde{\tau}_0$, $p_R^{(a)}(t; \tilde{\tau}_0)$ and $p_R^{(b)}(t; \tilde{\tau}_0)$ are non-overlapping in time. Accordingly, we divide $\mathbf{r}(t)$ into two disjoint parts in time as well: $\mathbf{r}(t)\text{rect}(t + T_s - \tilde{\tau}_0)$ for $t \in [0, \tilde{\tau}_0)$ and $\mathbf{r}(t)\text{rect}(t - \tilde{\tau}_0)$ for $t \in [\tilde{\tau}_0, T_s)$. The circularly shifted waveforms $p_R^{(a)}(t; \tilde{\tau}_0)$ and $p_R^{(b)}(t; \tilde{\tau}_0)$ can thus be estimated separately. Specifically, the objective function for $p_R^{(a)}(t; \tilde{\tau}_0)$ is [c.f. (6)]:

$$J^{(a)}(t; \tilde{\tau}_0) = 2\sqrt{\mathcal{E}} \mathbf{r}^T(t) \mathbf{s}_1 p_R^{(a)}(t; \tilde{\tau}_0) - \mathcal{E} \left\| \mathbf{s}_1 p_R^{(a)}(t; \tilde{\tau}_0) \right\|^2, \quad t \in [0, \tilde{\tau}_0).$$

Taking the derivative of $J^{(a)}(t; \tilde{\tau}_0)$ with respect to the instantaneous $p_R^{(a)}(t; \tilde{\tau}_0)$, and setting it to zero, we have the ML estimate of $p_R^{(a)}(t; \tilde{\tau}_0)$:

$$\hat{p}_R^{(a)}(t; \tilde{\tau}_0) = \frac{1}{K\sqrt{\mathcal{E}}} \sum_{k=1}^K s_{k-1} r_k(t) \text{rect}(t + T_s - \tilde{\tau}_0), \quad t \in [0, \tilde{\tau}_0). \quad (7)$$

Likewise, the ML estimate of $p_R^{(b)}(t; \tilde{\tau}_0)$ can be obtained by maximizing the following objective function [c.f. (6)]:

$$J^{(b)}(t; \tilde{\tau}_0) = 2\sqrt{\mathcal{E}} \mathbf{r}^T(t) \mathbf{s}_2 p_R^{(b)}(t; \tilde{\tau}_0) - \mathcal{E} \left\| \mathbf{s}_2 p_R^{(b)}(t; \tilde{\tau}_0) \right\|^2, \quad t \in [\tilde{\tau}_0, T_s),$$

and the resultant estimate is:

$$\hat{p}_R^{(b)}(t; \tilde{\tau}_0) = \frac{1}{K\sqrt{\mathcal{E}}} \sum_{k=1}^K s_k r_k(t) \text{rect}(t - \tilde{\tau}_0), \quad t \in [\tilde{\tau}_0, T_s). \quad (8)$$

In the second stage, we plug (7) and (8) back into (6), and discard the norm square term whose integral is not affected by the candidate $\tilde{\tau}_0$. It turns out that the new ML objective function for $\tilde{\tau}_0$ becomes:

$$\begin{aligned} J^{\text{ML}}(\tilde{\tau}_0) &= \frac{1}{K^2} \int_0^{T_s} \left(\mathbf{r}^T(t) \mathbf{s}_1 \sum_{k=1}^K s_{k-1} r_k(t) \text{rect}(t + T_s - \tilde{\tau}_0) + \mathbf{r}^T(t) \mathbf{s}_2 \sum_{k=1}^K s_k r_k(t) \text{rect}(t - \tilde{\tau}_0) \right) dt \\ &= \frac{1}{K^2} \sum_{m=1}^K \sum_{k=1}^K \int_0^{T_s} (r_m(t) r_k(t) s_{m-1} s_{k-1} \text{rect}(t + T_s - \tilde{\tau}_0) + r_m(t) r_k(t) s_m s_k \text{rect}(t - \tilde{\tau}_0)) dt, \quad (9) \end{aligned}$$

and the ML estimate of τ_0 can be obtained by maximizing $J^{\text{ML}}(\tilde{\tau}_0)$:

$$\hat{\tau}_0 = \arg \max_{\tilde{\tau}_0} J^{\text{ML}}(\tilde{\tau}_0) . \quad (10)$$

Proposition 1 [ML Timing Estimation] *The ML timing estimator can be implemented in four steps:*

- *Step 1: Take K received segments $r_k(t)$, $k = 1, 2, \dots, K$;*
- *Step 2: For each candidate $\tilde{\tau}_0$ calculate K^2 cross (and auto) correlations among all pairs of the segments as in (9);*
- *Step 3: Average the K^2 correlations as suggested by (9);*
- *Step 4: Choose the $\tilde{\tau}_0$ which maximizes $J^{\text{ML}}(\tilde{\tau}_0)$ as the ML estimate $\hat{\tau}_0$ according to (10).*

From Proposition 1 one should be aware that the computational complexity of the ML timing estimator is very high. For each $\tilde{\tau}_0$ candidate, one need to calculate K^2 correlations and K^2 summations. The high complexity is expected to be reduced for practical implementation.

C.2.2 Acquisition Performance of the ML timing Algorithm

In order to evaluate the performance of the ML estimator, we need to find the statistical properties of the objective function. Re-express $J^{\text{ML}}(\tilde{\tau}_0)$ as the sum of its noise-free part and noise term as $J^{\text{ML}}(\tilde{\tau}_0) = J_0^{\text{ML}}(\tilde{\tau}_0) + \xi^{\text{ML}}(\tilde{\tau}_0)$. Let us first consider the noise-free part

$$J_0^{\text{ML}}(\tilde{\tau}_0) = \frac{1}{K^2} \sum_{m,k=1}^K \int_0^{T_s} (\rho_m(t)\rho_k(t)s_{m-1}s_{k-1}\text{rect}(t + T_s - \tilde{\tau}_0) + \rho_m(t)\rho_k(t)s_m s_k \text{rect}(t - \tilde{\tau}_0)) dt \quad (11)$$

where $\rho_k(t)$ denotes the signal part of $r_k(t)$. Assuming the candidate $\tilde{\tau}_0 < \tau_0$ WLOG, we further define $\mathcal{E}_{A1} \triangleq \sqrt{\mathcal{E}} \int_0^{T_s - \tau_0} p_R^2(t) dt$, $\mathcal{E}_{A2}(\tilde{\tau}_0) \triangleq \sqrt{\mathcal{E}} \int_{T_s - \tau_0}^{T_s - \tau_0 + \tilde{\tau}_0} p_R^2(t) dt$, and $\mathcal{E}_B(\tilde{\tau}_0) \triangleq \sqrt{\mathcal{E}} \int_{T_s - \tau_0 + \tilde{\tau}_0}^{T_s} p_R^2(t) dt$. Then (11) becomes

$$\begin{aligned} J_0^{\text{ML}}(\tilde{\tau}_0) &= \frac{1}{K^2} \sum_{m,k=1}^K (s_m^2 s_k^2 \mathcal{E}_{A1} + s_{m-1}^2 s_{k-1}^2 \mathcal{E}_{A2}(\tilde{\tau}_0) + s_{m-1} s_m s_{k-1} s_k \mathcal{E}_B(\tilde{\tau}_0)) \\ &= \frac{1}{K^2} \sum_{m,k=1}^K (\mathcal{E}_A(\tilde{\tau}_0) + s_{m-1} s_m s_{k-1} s_k \mathcal{E}_B(\tilde{\tau}_0)) \end{aligned} \quad (12)$$

where $\mathcal{E}_A(\tilde{\tau}_0) \triangleq \mathcal{E}_{A1} + \mathcal{E}_{A2}(\tilde{\tau}_0)$. Notice that $\mathcal{E}_A(\tilde{\tau}_0) + \mathcal{E}_B(\tilde{\tau}_0) = \mathcal{E} \int_0^{T_s} p_R^2(t) dt = \mathcal{E}_R$ is the unknown but constant energy of a received segment independent of the trial value $\tilde{\tau}_0$. The noise-free part of the objective function can thus be simplified as

$$J_0^{\text{ML}}(\tilde{\tau}_0) = \mathcal{E}_R - \frac{\Delta_K}{K^2} \mathcal{E}_B(\tilde{\tau}_0), \quad (13)$$

where $\Delta_K \triangleq \sum_{m,k=1}^K (1 - s_{m-1} s_m s_{k-1} s_k)$ is a positive (as long as not all $s_{m-1} s_m s_{k-1} s_k = 1, \forall m, k$, which can be easily avoided.) parameter determined by the transmitted pilot sequence. By definition, the condition of correct timing $\tilde{\tau}_0 = \tau_0$ ensures that $\mathcal{E}_B(\tilde{\tau}_0)$ vanishes and $J_0^{\text{ML}}(\tilde{\tau}_0)$ achieves its unique maximum \mathcal{E}_R . Notice that since Δ_K is a sum of K^2 constants, its value is on the order of K^2 , or can be explicitly written as αK^2 , where α is a constant.

We now go to the noise term $\xi^{\text{ML}}(\tilde{\tau}_0)$. It can be proved that $\xi^{\text{ML}}(\tilde{\tau}_0)$ is Gaussian distributed with mean and variance:

$$\text{E}\{\xi^{\text{ML}}(\tilde{\tau}_0)\} = \frac{N_0 T_s}{2K}, \quad \text{var}\{\xi^{\text{ML}}(\tilde{\tau}_0)\} = \frac{2N_0 J_0^{\text{ML}}(\tilde{\tau}_0)}{K} + \frac{N_0^2 B T_s}{K^2}. \quad (14)$$

Then, one can obtain the mean and variance of the overall Gaussian ML objective function:

$$\begin{aligned} \text{E}\{J^{\text{ML}}(\tilde{\tau}_0)\} &= J_0^{\text{ML}}(\tilde{\tau}_0) + \text{E}\{\xi^{\text{ML}}(\tilde{\tau}_0)\} = J_0^{\text{ML}}(\tilde{\tau}_0) + \frac{N_0 T_s}{2K}, \\ \text{var}\{J^{\text{ML}}(\tilde{\tau}_0)\} &= \text{var}\{\xi^{\text{ML}}(\tilde{\tau}_0)\} = \frac{2N_0 J_0^{\text{ML}}(\tilde{\tau}_0)}{K} + \frac{N_0^2 B T_s}{K^2}. \end{aligned} \quad (15)$$

As one can see from (15), $J^{\text{ML}}(\tilde{\tau}_0)$ asymptotically converges to $J_0^{\text{ML}}(\tilde{\tau}_0)$ as $K \rightarrow \infty$, suggesting the optimality of the ML estimator.

We adopt the probability of detection lower bound \underline{P}_d to evaluate the coarse timing (acquisition) performance of the ML algorithm. Instead of estimating the true τ_0 , coarse timing aims at finding n_0 such that $|n_0 T_i - \tau_0| < T_i$, where T_i is the searching step size in the ML algorithm. Correspondingly, the maximization problem in (10) becomes:

$$\hat{n}_0 = \arg \max_{\tilde{n}_0} J^{\text{ML}}(\tilde{n}_0 T_i) \quad (16)$$

and the probability of detection is given by

$$\underline{P}_d^{\text{ML}} = \Pr\{\hat{n}_0 = n_0\} = \Pr\{\max_{\tilde{n}_0} J^{\text{ML}}(\tilde{n}_0 T_i) = J^{\text{ML}}(n_0 T_i)\}. \quad (17)$$

Since $J^{\text{ML}}(n_0 T_i)$ is Gaussian distributed, the lower bound of (17) is given by

$$\underline{P}_d^{\text{ML}} = \prod_{\tilde{n}_0 \neq n_0} F \left(\frac{\text{E}\{J^{\text{ML}}(n_0 T_i)\} - \text{E}\{J^{\text{ML}}(\tilde{n}_0 T_i)\}}{\sqrt{\text{var}\{J^{\text{ML}}(n_0 T_i)\} + \text{var}\{J^{\text{ML}}(\tilde{n}_0 T_i)\}}} \right) \quad (18)$$

where $F(\cdot)$ is the cumulative distribution function (cdf) of Gaussian distribution with zero mean and unit variance.

Substituting the mean and variance of the objective function given in (15), we can obtain the probability of detection lower bound:

$$\underline{P}_d^{\text{ML}} = \prod_{\tilde{n}_0 \neq n_0} F\left(\frac{\Delta_K \mathcal{E}_B(\tilde{n}_0 T_i)}{\sqrt{4N_0 \mathcal{E}_R K^3 - 2N_0 \Delta_K \mathcal{E}_B(\tilde{n}_0 T_i) K + 2N_0^2 B T_s K^2}}\right). \quad (19)$$

Remarks: i) As K increases the variance of the objective function decreases and the probability of detection lower bound increases. This suggests that the timing performance would benefit from more correlation averaging; and ii) As Δ_K increases the variance of the objective function is reduced and the probability of detection lower bound increases. Intuitively, (13) provides another evidence that the objective function becomes sharper along with the increase of Δ_K , making detection of n_0 easier. Since Δ_K is determined by the transmitted symbol sequence, one can expect that the acquisition performance would be markedly improved by optimizing the training sequence such that Δ_K is maximized.

C.3 Training Sequence Design and The SML Algorithm

C.3.1 The Optimum Training Sequence Pattern

The value of $\Delta_K = \sum_{m,k=1}^K (1 - s_{m-1} s_m s_{k-1} s_k)$ is determined by the signs of the consecutive symbols. Define $c_k \triangleq s_{k-1} s_k \in \{\pm 1\}, k = 1, \dots, K$, as the product of two consecutive symbols. Then c_k belongs to one of the two groups, $\Gamma_+ \triangleq \{c_k, \forall k : c_k = 1\}$ with cardinality K_+ and $\Gamma_- \triangleq \{c_k, \forall k : c_k = -1\}$ with cardinality K_- . Evidently, $K_+ + K_- = K$.

Lemma 1 *For a specific K , $\max\{\Delta_K\} = K^2$ is achieved when $K_+ = K_- = K/2$; that is, half of the $\{c_k\}_k$ elements belong to Γ_+ and the other half belong to Γ_- .*

Notice that we only considered even K WLOG, since odd K has the same maximization result with its even neighbor $K - 1$.

Lemma 1 gives the condition that maximizes Δ_K for a particular K . Additionally, the optimum training sequence should also be consistent; that is, applicable to arbitrary K . To this end, we first notice that the ML timing estimator requires $K \geq 2$, since when $K = 1$, $J_0^{\text{ML}}(\tilde{\tau}_0) = \mathcal{E}_R$ [c.f. (12)] is simply a constant and gives no information about τ_0 . Following Lemma 1, the consistency property can be ensured $\forall K \geq 2$ by: i) partitioning the $\{c_k\}_k$ sequence into doublets $\{c_{2n-1} c_{2n}\}, n = 1, 2, \dots, K/2$; and ii) making sure that each $\{c_{2n-1} c_{2n}\}$

doublet contains a “+1” and a “−1”, i.e., each doublet should be either $\{+1, -1\}$ or $\{-1, +1\}$. With this condition, the $\{c_k\}_k$ sequence always has $K_+ = K_-$ regardless of K . Note that, the $K = 2$ case which ensures rapid acquisition using only 2 segments is a natural corollary of the consistency property.

In addition, to guarantee that the “+1”, “−1” pairing condition holds for any doublet starting from odd- and even-indexed symbols, all the doublets should be identical. In other words, they are either all $\{+1, -1\}$ or all $\{-1, +1\}$. As a result, this gives rise to a *unique* training sequence $\{s_k\}_k$ consisting of the repeated pattern $\{+1, +1, -1, -1\}$ (or its circularly shifted versions). We summarize the analysis in the following result:

Proposition 2 [Optimum Training Sequence] *The unique optimum training sequence for the ML estimator has the structure*

$$s_k = (-1)^{\lfloor k/2 \rfloor}, \quad (20)$$

which ensures rapid acquisition using as few as 3 symbols and is applicable to arbitrary $K(\geq 2)$.

C.3.2 Simplified ML (SML) Algorithm

For simplicity, denote the integrals in the objective function for $\tilde{\tau}_0$ (9) as $j_{m,k}$. Considering the partition of the training sequence by groups Γ_+ and Γ_- , we can rewrite (9) as

$$J^{\text{ML}}(\tilde{\tau}_0) = \frac{1}{K^2} \left\{ \sum_{\{(m,k):c_m,c_k \in \Gamma_+\}} j_{m,k} + \sum_{\{(m,k):c_m,c_k \in \Gamma_-\}} j_{m,k} \right. \\ \left. + \sum_{\{(m,k):c_m \in \Gamma_+,c_k \in \Gamma_-\}} j_{m,k} + \sum_{\{(m,k):c_m \in \Gamma_-,c_k \in \Gamma_+\}} j_{m,k} \right\}. \quad (21)$$

Consider the first two summations. Since c_m and c_n are chosen from the same group (namely Γ_+ in the first summation and Γ_- in the second summation), the noise-free parts of the summands are exclusively $\mathcal{E}_A(\tilde{\tau}_0) + \mathcal{E}_B(\tilde{\tau}_0) = \mathcal{E}_R$ [c.f.(12)]. Furthermore, it is not difficult to verify that the noise terms in the first two summations do not change with the shift candidate $\tilde{\tau}_0$. Therefore, the first two summations are nothing but constants, which provide no information on τ_0 . If one knows which (c_m, c_k) pairs give rise to these summands, one can avoid calculating their corresponding cross correlations.

The optimum training sequence given by (20) precisely allows one to achieve this. The repeated pattern $\{+1, +1, -1, -1\}$ indicates that the received K symbol-long segments can

be divided into two groups by simply checking their indices. Specifically, if the symbol-long received segment with odd index $r_{2k-1}(t)$ carries two successive symbols satisfying $c_{2k-1} = s_{2k-2}s_{2k-1} \in \Gamma_+$ (or Γ_-), then the symbol-long received segment with even index r_{2k} must carry two successive symbols satisfying $c_{2k} = s_{2k-1}s_{2k} \in \Gamma_-$ (or Γ_+). Retaining only the cross correlations between the two groups, we can obtain the simplified ML (SML) objective function as

$$J^{\text{SML}}(\tilde{\tau}_0) = \frac{2}{K^2} \sum_{m,k=1}^{K/2} j_{m,k}^{\text{SML}},$$

$$j_{m,k}^{\text{SML}} = \int_0^{T_s} r_{2m-1}(t)r_{2k}(t)(-1)^{\lfloor \frac{2m-2}{2} \rfloor}(-1)^{\lfloor \frac{2k-1}{2} \rfloor} \text{rect}(t+T_s-\tilde{\tau}_0) \\ + r_{2m-1}(t)r_{2k}(t)(-1)^{\lfloor \frac{2m-1}{2} \rfloor}(-1)^{\lfloor \frac{2k}{2} \rfloor} \text{rect}(t-\tilde{\tau}_0) dt. \quad (22)$$

Note that the last two summation terms in (21) are exactly the same, which explains the reason why a scaling coefficient 2 shows up in (22).

We can rewrite $J^{\text{SML}}(\tilde{\tau}_0)$ by putting the double summations into the integral:

$$J^{\text{SML}}(\tilde{\tau}_0) = \frac{1}{2} \int_0^{T_s} \left(\frac{2}{K} \sum_{m=1}^{K/2} (-1)^m r_{2m-1}(t) \right) \left(\frac{2}{K} \sum_{k=1}^{K/2} (-1)^k r_{2k}(t) \right) \\ \cdot (\text{rect}(t+T_s-\tilde{\tau}_0) - \text{rect}(t-\tilde{\tau}_0)) dt. \quad (23)$$

The above integrand includes the product of three terms. The first is the average of the odd indexed received segments which satisfies the condition for the group Γ_+ ; the second is the average of those even indexed received segments falling into the group Γ_- ; and the last term is the window function accounting for the guess shift $\tilde{\tau}_0$.

Proposition 3 [SML Timing Estimation] *By employing the optimum training sequence given in Proposition 2, the SML estimator can be implemented with much lower complexity than the ML estimator:*

- Step 1: Take K received segments $r_k(t), \forall k$;
- Step 2: Average the odd and even indexed segments respectively as suggested by (23);
- Step 3: For each candidate $\tilde{\tau}_0$, form the window functions $\text{rect}(t+T_s-\tilde{\tau}_0)$ and $-\text{rect}(t-\tilde{\tau}_0)$, and calculate $J^{\text{SML}}(\tilde{\tau}_0)$ as (23);

- *Step 4: Choose the $\tilde{\tau}_0$ which maximizes $J^{\text{SML}}(\tilde{\tau}_0)$ as the SML estimate $\hat{\tau}_0$; that is, $\hat{\tau}_0 = \arg \max_{\tilde{\tau}_0} J^{\text{SML}}(\tilde{\tau}_0)$.*

It is important to note that the complexity of the SML timing estimator is significantly reduced. One only needs to evaluate K summations and 1 correlation for each $\tilde{\tau}_0$ candidate. Moreover, in a digital implementation, we do not need to compute the correlation for every new $\tilde{\tau}_0$, as most of the correlation is identical from the current $\tilde{\tau}_0$ value to the next. Additional computing saving can be obtained by only updating the difference instead of calculating every correlation anew.

Like the ML estimator, we are also interested in the acquisition performance of the SML estimator. Inherited from (12) with $s_{2m-2}s_{2m-1}s_{2k-1}s_{2k} = -1, \forall m, k$, the noise-free part of the SML objective function in (22) can be expressed as:

$$J_0^{\text{SML}}(\tilde{\tau}_0) = \frac{\mathcal{E}_A(\tilde{\tau}_0) - \mathcal{E}_B(\tilde{\tau}_0)}{2} = \frac{\mathcal{E}_R - 2\mathcal{E}_B(\tilde{\tau}_0)}{2}. \quad (24)$$

The noise term $\xi^{\text{SML}}(\tilde{\tau}_0)$ is Gaussian distributed with zero mean and variance (the proof is similar to that for the ML, thus omitted here):

$$\text{var}\{\xi^{\text{SML}}(\tilde{\tau}_0)\} = \frac{N_0\mathcal{E}_R}{2K} + \frac{N_0^2BT_s}{2K^2}. \quad (25)$$

After calculating the mean and variance for $J^{\text{SML}}(\tilde{\tau}_0)$:

$$\text{E}\{J^{\text{SML}}(\tilde{\tau}_0)\} = \frac{\mathcal{E}_A(\tilde{\tau}_0) - \mathcal{E}_B(\tilde{\tau}_0)}{2}, \quad \text{var}\{J^{\text{SML}}(\tilde{\tau}_0)\} = \frac{N_0\mathcal{E}_R}{2K} + \frac{N_0^2BT_s}{2K^2}, \quad (26)$$

we obtain the probability of detection lower bound for the SML algorithm as:

$$P_d^{\text{SML}} = \prod_{\tilde{n}_0 \neq n_0} F\left(\frac{K\mathcal{E}_B(\tilde{n}_0T_i)}{\sqrt{KN_0\mathcal{E}_R + N_0^2BT_s}}\right). \quad (27)$$

C.4 Implementation Considerations and Simulated Performance

Theoretically, the SML algorithm can always detect n_0 such that $|n_0T_i - \tau_0| < T_i$ on any resolution level T_i as long as the complexity of the receiver is allowed. In practice, however, significant attenuation at the tail of a multipath channel and the extent of noise-only region between consecutive symbols make things more complicated. The unique peak at n_0 of the objective function tends to be comparable with its left neighbors $\tilde{n}_0 < n_0$ even when the noise is absent. Therefore, the correct timing of $\tilde{n}_0 = n_0$ with fine (e.g., chip-level) resolution is not easily distinguishable as the peak. On the other hand, we notice that the value of the

objective function decreases dramatically for $\tilde{n}_0 > n_0$, as a result of the first few strong taps of the channel. Thanks to the different behavior of the regions $\tilde{n}_0 < n_0$ and $\tilde{n}_0 > n_0$, one can resort to the first-order difference of the objective function in aid of finding n_0 at chip level.

Suppose that the frame-level acquisition has already been achieved. After obtaining the values of $J(\tilde{n}_0 T_c)$ in the right frame where n_0 is located, take the difference $\Delta J(\tilde{n}_0 T_c) = J(\tilde{n}_0 T_c) - J(\tilde{n}_0 T_c - w T_c)$, where $w \in [1, N_c]$ and $w T_c$ denotes the step size. Then the candidate \tilde{n}_0 which maximizes $\Delta J(\tilde{n}_0 T_c)$ will be regarded as the estimate of n_0 .

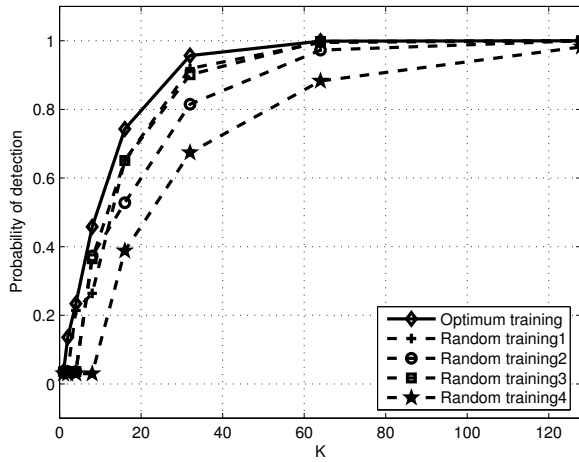
We use the channel model IEEE 802.15.3a CM1 to generate the multipath channel. The UWB pulse is the second derivative of the Gaussian function with unit energy and duration $T_p \approx 1$ ns. The frame duration is $T_f = 35$ ns, and each symbol contains $N_f = 32$ frames. A random time hopping code c_j is uniformly distributed over $[0, N_c - 1]$, with $N_c = 35$ and $T_c = 1$ ns. To avoid ISI, the time hopping code for the last frame of each symbol is set to $c_{N_f-1} = 0$.

Test 1 illustrates the optimality of the training sequence given in (20) for the ML estimator. Fig. 1(a) compares the optimum training pattern with four randomly chosen sequences. We can observe that for $K = 2$ only the optimum training sequence works. With $K > 2$, although the other four can also work, the optimum training sequence consistently provides the best performance for any K . We will employ the optimum training sequence in the subsequent simulations.

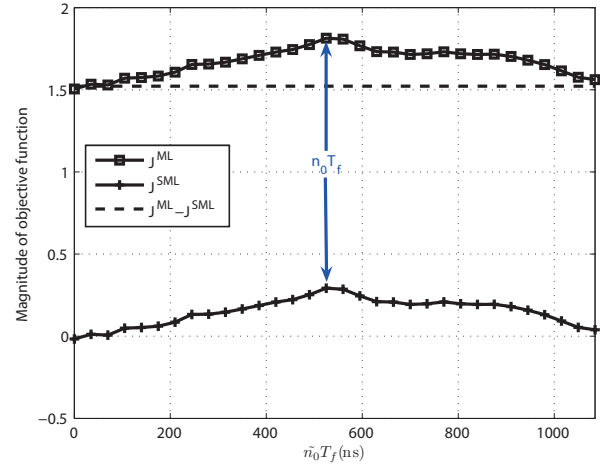
Test 2 plots the objective functions of the ML and SML algorithms in one realization at the frame level in Fig. 1(b). For comparison, the corresponding noise-free part of the SML (and TDT) algorithm is also provided. It is shown that the ML and SML objective functions have identical shape. The difference between them remains the same for all candidates \tilde{n}_0 .

Test 3 depicts the acquisition performance of the SML algorithm. The probabilities of detection, together with the analytical lower bounds (27) are plotted in Fig. 2(a). The normalized mean square errors (MSE), which are normalized with respect to T_s^2 , are also shown in Fig. 2(b).

Test 4 is designed to show the chip-level fine timing performance. The frame-level acquisition is assumed to be achieved beforehand. As illustrated in Fig. 3(a), the performance of the difference operation depends on the step size $w T_c$. Accordingly, we choose the optimum value for CM1 in our simulation as $w T_c = 3$ ns at low SNR and $w T_c = 8$ ns at high SNR. The normalized MSE for the SML algorithm with various K is plotted in Fig. 3(b). Notice that all curves reach an error floor since the timing with chip-level resolution is performed.

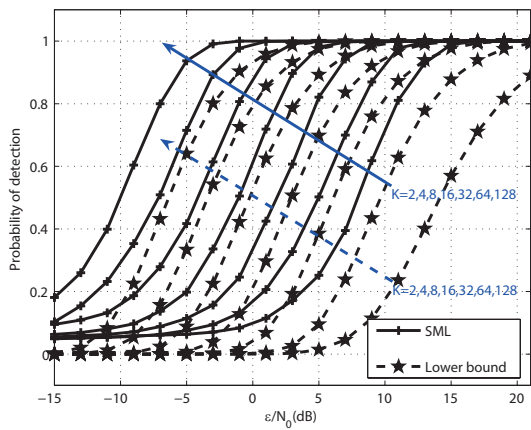


(a)

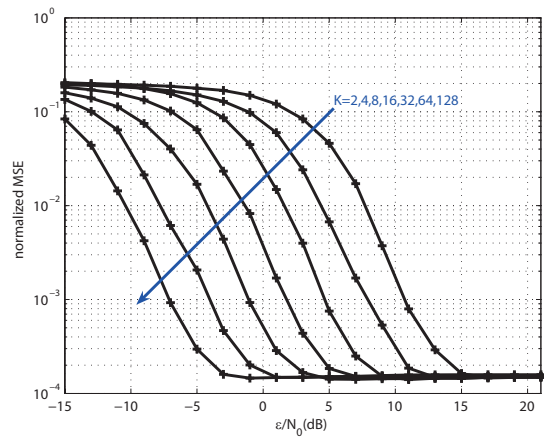


(b)

Figure 1: (a) P_d for various sequences, $\mathcal{E}/N_0 = 1dB$. (b) Objective function magnitude for the ML and SML algorithms, $\mathcal{E}/N_0 = 5dB$, $K = 8$ and $n_0 = 15$.



(a)



(b)

Figure 2: (a) P_d and \underline{P}_d for the SML algorithm, coarse timing. (b) Normalized MSE for the SML algorithm, coarse timing.

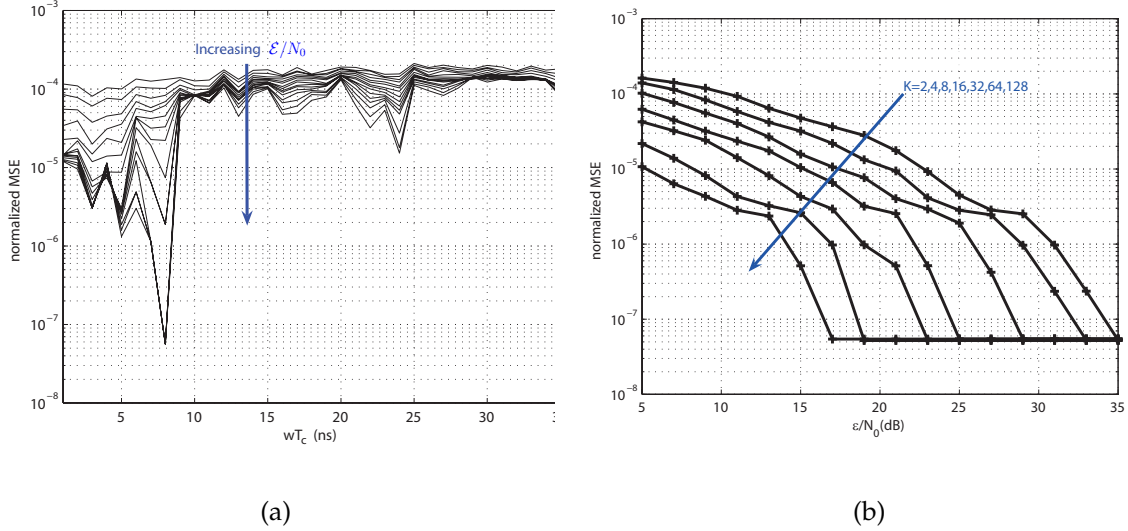


Figure 3: (a) Normalized MSE versus differential step wT_c under various E/N_0 . (b) Normalized MSE for the SML algorithm, fine timing.

C.5 Summary

In this research, we developed the data-aided ML timing algorithm, and derived the optimum training sequence for the ML algorithm. Based on this optimum sequence, the original ML algorithm can be simplified without affecting its optimality. Extensive simulations have been performed to corroborate our theoretical analysis.

D Ranging with Single-Band UWB Signals: Focusing-on-First-arrival (FoFa)

In the literature, various techniques have been proposed for ToA estimation for broadband wireless systems. A straightforward method is to capture the first signal arrival by a sliding correlator with a locally generated template at the receiver. In order to achieve high-accuracy channel estimation and consequently high-accuracy ToA estimation, the correlator has to slide at a sufficiently small step size. This implies either very long search time or very high complexity receiver, depending on whether the correlations are performed in serial or parallel.

In order to avoid the sliding correlator required in the time domain approaches, frequency domain alternatives were proposed for ToA estimation, which are typically based

on the frequency domain equalization (FDE) framework. This type of techniques treat ToA estimation as a by-product of channel estimation. Intuitively, if one obtains all channel parameters including each path's gain and delay, then the delay of the first multipath arrival automatically becomes the ToA estimate. Using the fast Fourier transform (FFT), FDE can be realized at a low complexity. For FDE systems, the frequency domain channel information should be converted to the time domain to facilitate ToA estimation. This conversion gives rise to various channel estimation techniques including the model-based estimator that models the channel as a tapped delay line structure, the space alternating generalized expectation maximization (SAGE) algorithm and the subspace-based estimator.

Problems arise when these channel estimators are employed for ToA estimation. Firstly, the fixed structure of the tapped delay line model can not match the contiguously changing tap delays. Secondly, the criterion used for channel estimation purpose is often either to maximize the likelihood or to minimize the estimation error between the estimates of all channel paths and the real ones. As a result, the contribution from the first path is very small, especially when there is a large number of dense multipath components. Hence, these approaches often encounter poor convergence or suffer from local optimum problems, when being used as ToA estimators.

To avoid these problems, we propose to estimate the ToA of the channel by *Focusing On the First Arrival*, which we term as FoFa. Compared to conventional methods, the FoFa ToA estimator has the following advantages. Firstly, FoFa uses the frequency domain channel information readily available in FDE systems to recover the time domain channel with an equally-spaced model, which can effectively reduce the complexity of the estimation. Secondly, unlike conventional ToA estimators, FoFa relies on a novel criterion to optimize the ToA estimation; that is, locating the first path by minimizing the energy leakage prior to the first path. As a result, FoFa directly addresses the delay estimation of the first channel path, without unnecessarily caring about the estimation errors for the trailing paths. This avoids the poor convergence and local optimum problems often encountered when treating ToA estimate as a by-product of channel estimation. In addition, all computations are carried out with the baseband signal instead of the analog or oversampled waveform. Therefore, the complexity of the FoFa ToA estimator is much lower than that of the sliding-correlator-based estimator.

Notation: We will use bold upper and lower cases to denote matrices and column vectors, respectively. We will use $(\cdot)^T$ and $(\cdot)^H$ for transpose and conjugate transpose of matrices

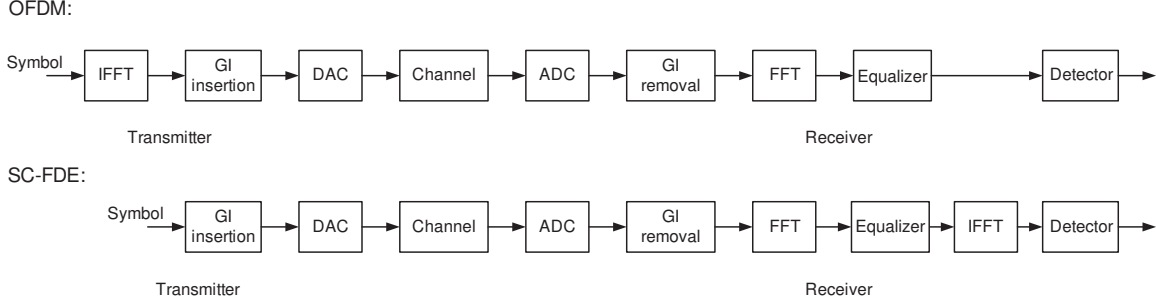


Figure 4: Baseband transceiver diagrams for OFDM and SC-FDE.

and vectors, and $(\cdot)^*$ for conjugate of complex numbers.

D.1 Broadband System Model with FDE

In this section, we will briefly review the FDE systems. Typical FDE systems include the well-known orthogonal frequency-division multiplexing (OFDM) system and the single-carrier frequency domain equalization (SC-FDE) system. Let us first explain the basic idea of OFDM systems, and then briefly introduce SC-FDE. At the OFDM transmitter (see Fig. 4), a block of information symbols $\mathbf{s} = [s_1, \dots, s_N]^T$ are multi-carrier modulated onto N orthogonal digital subcarriers to form $\mathbf{x} = \mathbf{F}^H \mathbf{s}$, where \mathbf{F} is the FFT matrix. A guard interval (GI) in the form of padding zeros (ZP) or cyclic prefix (CP) is added to each block to mitigate the inter-symbol interference (ISI). After the digital-to-analog conversion (DAC), the signal is carrier modulated and transmitted from the antenna. The transmitted signal then propagate through the channel: $h(t) = \sum_{l=1}^L h_l \cdot \delta(t - \tau_l)$, where $\{h_l\}_{l=1}^L$ and $\{\tau_l\}_{l=1}^L$ are amplitudes and delays of the L channel paths, respectively. Note that we do not require $\{\tau_l\}_{l=1}^L$ to be equally spaced and do not assume any *a priori* channel information.

At the receiver, the arriving waveform is carrier demodulated and analog-to-digital (A/D) converted to baseband discrete-time samples. After the GI is removed, the baseband signal is multi-carrier demodulated with FFT operation to generate sequence $\{r_k\}_{k=1}^N$. With some coarse synchronization, it can be easily shown that

$$r_k = s_k H_k + w_k, \quad k = 1, \dots, N, \quad (28)$$

where w_k is the additive white Gaussian noise (AWGN), and $\{H_k\}_{k=1}^N$ are the Fourier transform (FT) coefficients of the channel:

$$H_k = \sum_{l=1}^L h_l \cdot \exp(-j\omega_k \tau_l), \quad \omega_k = 2k\pi/T_B, \quad (29)$$

where T_B is the information block duration. Based on (28), the maximum likelihood (ML) estimate of H_k can be formed as $\hat{H}_k = r_k/s_k$, $1 \leq k \leq N$.

Fig. 4 compares the baseband block diagrams of OFDM and SC-FDE. The difference between OFDM and SC-FDE is where the IFFT operation is performed. In OFDM, IFFT is adopted at the transmitter to modulate information symbols on subcarriers. In SC-FDE, IFFT is performed at the receiver to convert the FDE output back to the time domain symbols.

D.2 Energy Leakage in Channel Estimate

Following the literature, the channel is estimated by fitting the equally-spaced model (30) to the frequency domain channel

$$\bar{h}(t) = \sum_{n=1}^{\bar{L}} \bar{h}_n \cdot \delta(t - \bar{\tau}_n) \quad (30)$$

where $\bar{\tau}_n = \bar{\tau}_1 + (n - 1)T_p$, $1 \leq n \leq \bar{L}$ and $\bar{L} = \lceil T_h/T_p \rceil$ with T_h being the maximum channel delay spread and T_p the tap interval which is chosen as the inverse of the signal bandwidth. By doing this, ToA of the channel can be estimated by optimizing the single free parameter $\bar{\tau}_1$. This is in comparison with existing channel estimators which search all individual channel path delays in $[0, T_h]$.

Given $\bar{\tau}_1$, $\{\bar{h}_n(\bar{\tau}_1)\}_{n=1}^{\bar{L}}$ are expected to satisfy [c.f. (29)]

$$\sum_{n=1}^{\bar{L}} \bar{h}_n(\bar{\tau}_1) \exp(-j\omega_{b,k}\bar{\tau}_n) = \hat{H}_{b,k} \quad (31)$$

where the dependance of $\{\bar{h}_n(\bar{\tau}_1)\}_{n=1}^{\bar{L}}$ on $\bar{\tau}_1$ is explicitly shown. More compactly written, we have

$$\mathbf{G}(\bar{\tau}_1)\bar{\mathbf{h}}(\bar{\tau}_1) = \mathbf{H} + \boldsymbol{\eta} \quad (32)$$

where $\mathbf{H} = [\mathbf{H}_1^T, \mathbf{H}_2^T, \dots, \mathbf{H}_B^T]^T$ and $\boldsymbol{\eta} = [\boldsymbol{\eta}_1^T, \boldsymbol{\eta}_2^T, \dots, \boldsymbol{\eta}_B^T]^T$ include all the subband FT coefficients and noise terms, respectively, $\bar{\mathbf{h}}(\bar{\tau}_1) = [\bar{h}_1(\bar{\tau}_1), \bar{h}_2(\bar{\tau}_1), \dots, \bar{h}_{\bar{L}}(\bar{\tau}_1)]^T$ and $\mathbf{G}(\bar{\tau}_1) = [\mathbf{G}_1^T(\bar{\tau}_1), \mathbf{G}_2^T(\bar{\tau}_1), \dots, \mathbf{G}_B^T(\bar{\tau}_1)]^T$ with $\mathbf{G}_b(\bar{\tau}_1)$ being a $K \times \bar{L}$ FT matrix with the (k, n) th element being $\exp(-j\omega_{b,k}\bar{\tau}_n)$. Based on Eq. (32), $\bar{\mathbf{h}}(\bar{\tau}_1)$ can be obtained by

$$\bar{\mathbf{h}}(\bar{\tau}_1) = (\mathbf{G}^H(\bar{\tau}_1)\mathbf{G}(\bar{\tau}_1))^{-1} \mathbf{G}^H(\bar{\tau}_1)\mathbf{H} + \bar{\boldsymbol{\eta}} \quad (33)$$

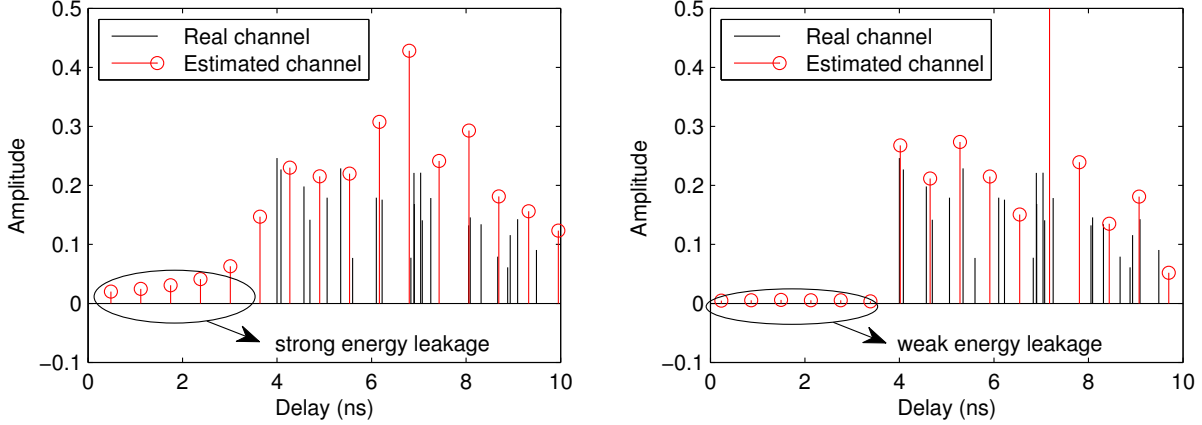


Figure 5: (a) Strong energy leakage. (b) Weak energy leakage.

where $\bar{\eta}$ is the noise.

From (29), the frequency domain channel response $H_{b,k}$ contains information from all L channel paths. Therefore, the channel estimate can also be expressed as

$$\bar{\mathbf{h}}(\bar{\tau}_1) = \sum_{l=1}^L (\mathbf{G}^{\mathcal{H}}(\bar{\tau}_1)\mathbf{G}(\bar{\tau}_1))^{-1} \mathbf{G}^{\mathcal{H}}(\bar{\tau}_1)\mathbf{H}(l) + \bar{\eta} \quad (34)$$

where $\mathbf{H}(l)$ is the frequency domain contribution from the l th channel path which can be constructed by $\mathbf{H}(l) = [\mathbf{H}_1^T(l), \mathbf{H}_2^T(l), \dots, \mathbf{H}_B^T(l)]^T$ and $\mathbf{H}_b(l) = [h_l \exp(-j\omega_{b,1}\tau_l), h_l \exp(-j\omega_{b,2}\tau_l), \dots, h_l \exp(-j\omega_{b,K}\tau_l)]^T$. Same as other ToA estimators for MB-OFDM, Eq. (33) also assumes that no random phase rotation exists in subband signals.

Proposition 4 For the l th channel path (h_l, τ_l) , given the channel estimator (33), only the m th tap of the channel estimate contains non-zero contribution from the l th path if this path is exactly sampled by the m th tap as $\tau_l = \bar{\tau}_m, \exists m \in [1, \bar{L}]$.

This is because when $\tau_l = \bar{\tau}_m$, $\mathbf{H}(l)$ will be the m th column of the matrix $\mathbf{G}(\bar{\tau}_1)$ scaled by h_l . Then, only the m th element in $(\mathbf{G}^{\mathcal{H}}(\bar{\tau}_1)\mathbf{G}(\bar{\tau}_1))^{-1}\mathbf{G}^{\mathcal{H}}(\bar{\tau}_1)\mathbf{H}(l)$ is non-zero (see Eq. (34)). If the l th channel path is missampled, i.e., $\tau_l \neq \bar{\tau}_n, \forall n \in [1, \bar{L}]$, all estimated channel taps $\{\bar{h}_n\}_{n=1}^{\bar{L}}$ are generally non-zero even if noise is absent. As a result, energy of this channel path will disperse into all taps. This is known as the *energy leakage* phenomenon. In a multipath channel with continuously varying path delays, the equally-spaced model can not simultaneously sample all channel paths. Therefore, energy leakage will always exist.

The tap interval T_p is set as the inverse of the signal bandwidth, which is known as

the time resolution of the system. When T_p is smaller, $\mathbf{G}^H(\bar{\tau}_1)\mathbf{G}(\bar{\tau}_1)$ in (33) tends to be ill-conditioned and the problem becomes unsolvable.

From Eq. (34), the n th estimated channel tap is the summation of contributions from all paths of the physical channel:

$$\bar{h}_n(\bar{\tau}_1) = \sum_{l=1}^L \bar{h}_n(\bar{\tau}_1, l) + \bar{\eta}_n(\bar{\tau}_1), \quad n = 1, \dots, \bar{L} \quad (35)$$

where $\bar{h}_n(\bar{\tau}_1, l)$ contains the information of the l th path and $\bar{\eta}_n(\bar{\tau}_1)$ is the noise. When T_p is chosen as the inverse of the signal bandwidth, $\bar{h}_n(\bar{\tau}_1, l)$ can be further expressed by

$$\begin{aligned} \bar{h}_n(\bar{\tau}_1, l) = & h_l \exp\left(\frac{j\pi(N-1)(\bar{\tau}_n - \tau_l)}{NT_p}\right) \\ & \times \frac{\sin(\pi(\bar{\tau}_n - \tau_l)/T_p)}{N \sin(\pi(\bar{\tau}_n - \tau_l)/(NT_p))}. \end{aligned} \quad (36)$$

Eq. (36) is actually the sampled version of the discrete sinc-function. Therefore, we have the following results.

Proposition 5 *The m th channel estimate tap contains the strongest energy from the l th channel path if $m = \arg \min_{1 \leq n \leq \bar{L}} |\tau_l - \bar{\tau}_n|$, i.e., $\{\bar{\tau}_m, \bar{h}_m\}$ is the closest tap to $\{\tau_l, h_l\}$. Given this, energy leakage on the other taps decreases as their tap indices n ($n \neq m$) deviate from m .*

Proposition 6 *Given that the m th estimated channel tap contains the strongest energy from $\{\tau_l, h_l\}$, $h_m(\bar{\tau}_1, l)$ increases as $|\tau_l - \bar{\tau}_m|$ decreases in $[0, T_p/2)$. Energy on the other taps $|\bar{h}_n(\bar{\tau}_1, l)|$, $n \neq m$ approximately decreases when $|\tau_l - \bar{\tau}_m|$ decreases in $[0, T_p/2)$.*

Figs. 5(a) and 5(b) use two different values of $\bar{\tau}_1$ to channel estimate. We can see that by using a proper $\bar{\tau}_1$, energy leakage prior to the first path $\{h_1, \tau_1\}$ can be much weaker.

D.3 The Proposed ToA Estimator

For the ToA estimation purpose, Fig. 5(b) is clearly more preferable than Fig. 5(a). This is because when the channel estimate in Fig. 5(a) is used by the threshold-based ToA estimator, one of the strong energy leakage taps can be mistakenly picked out as the first path. This may cause a severe ToA estimation error. Therefore, we need to suppress the energy leakage before estimating the ToA.

When the energy leakage is sufficiently suppressed, a sharp jump of the tap amplitude will emerge near the leading edge of the channel (see Fig. 5(b)). This sharp jump of amplitude can be detected by searching the value of $\bar{\tau}_1$ to maximize the following energy ratio between two adjacent taps

$$\gamma_n(\bar{\tau}_1) = \frac{|\bar{h}_n(\bar{\tau}_1)|^2}{|\bar{h}_{n-1}(\bar{\tau}_1)|^2}, n \in [L_1, L_2] \quad (37)$$

where $[L_1, L_2]$ represents the remaining ToA estimation error after coarse timing. The ToA estimate is then obtained by:

$$\hat{\tau}_1 = \hat{\tau}_1 + (\hat{n} - 1)T_p \quad (38)$$

with $(\hat{\tau}_1, \hat{n}) = \underset{0 \leq \bar{\tau}_1 < T_h, L_1 \leq n \leq L_2}{\operatorname{argmax}} \gamma_n(\bar{\tau}_1)$. The advantage of this criterion is that it avoids the channel dependent threshold required by the threshold-based ToA estimators.

D.3.1 Analysis of ToA Estimation Criterion

Analysis of Eq. (35) for an arbitrary multipath channel is mathematically intractable. Therefore, we consider a simplified two-path channel with the inter-path interval being $(p+0.5)T_p$ and p an integer. In this model, the first path carries the ToA information and the second path models the interference from trailing paths. For this case, the strongest interference arises from the second path when the first path is sampled at its true arrival instant.

Suppose that the channel paths have amplitudes $[h_1, h_2]$ and delays $[\tau_1, \tau_2]$. Then the energy ratio given by Eq. (37) can be expressed as

$$\gamma_n(\bar{\tau}_1) = \frac{|\bar{h}_n(\bar{\tau}_1, 1) + \bar{h}_n(\bar{\tau}_1, 2)|^2}{|\bar{h}_{n-1}(\bar{\tau}_1, 1) + \bar{h}_{n-1}(\bar{\tau}_1, 2)|^2}, n \in [L_1, L_2] \quad (39)$$

where $\bar{h}_n(\bar{\tau}_1, 1)$ and $\bar{h}_n(\bar{\tau}_1, 2)$ are contributions from the two channel paths [c.f. (36)].

Using $\tau_2 = (p + 0.5)T_p + \tau_1$ and $\exp(j\pi(p + 0.5)T_p/(NT_p)) \approx 1$ when $p \ll N$, we have

$$\begin{aligned} \bar{h}_n(\bar{\tau}_1, 2) &\approx \bar{h}_n(\bar{\tau}_1, 1) \frac{h_2(-1)^p j}{h_1} \\ &\times \frac{\sin(\pi(\bar{\tau}_n - \tau_1)/(NT_p)) \sin(\pi(\bar{\tau}_n - \tau_2)/T_p)}{\sin(\pi(\bar{\tau}_n - \tau_1)/T_p) \sin(\pi(\bar{\tau}_n - \tau_2)/(NT_p))}. \end{aligned} \quad (40)$$

Therefore, energy of the n th tap can be approximated by $|\bar{h}_n(\bar{\tau}_1)|^2 = |\bar{h}_n(\bar{\tau}_1, 1)|^2 + |\bar{h}_n(\bar{\tau}_1, 2)|^2$ and the energy ratio can be expressed as

$$\gamma_n(\bar{\tau}_1) = \frac{|\bar{h}_n(\bar{\tau}_1, 1)|^2 + |\bar{h}_n(\bar{\tau}_1, 2)|^2}{|\bar{h}_{n-1}(\bar{\tau}_1, 1)|^2 + |\bar{h}_{n-1}(\bar{\tau}_1, 2)|^2}, n \in [L_1, L_2]. \quad (41)$$

Since Eq. (41) is still too complicated to analyze, we need to further simplify it. Suppose that $|\bar{h}_n(\bar{\tau}_1, 1)|$ and $|\bar{h}_n(\bar{\tau}_1, 2)|$ reach their maximum values at the m th and m' th taps ($m < m'$), respectively, such that $|\bar{h}_m(\bar{\tau}_1, 1)| = \max(|\bar{h}_n(\bar{\tau}_1, 1)|)$ and $|\bar{h}_{m'}(\bar{\tau}_1, 2)| = \max(|\bar{h}_{n'}(\bar{\tau}_1, 2)|)$, $n, n' \in [1, \bar{L}]$. Numerical analysis has confirmed that the energy ratio will only be maximized at the m th and m' th taps of the estimated channel. Based on this, the ToA estimate will be either $\bar{\tau}_m$ or $\bar{\tau}_{m'}$. From Proposition 5, we know that $|\tau_1 - \bar{\tau}_m| \in [0, T_p/2)$ and $|\tau_2 - \bar{\tau}_{m'}| \in [0, T_p/2)$. Certainly, we prefer $\bar{\tau}_m$ than $\bar{\tau}_{m'}$. We will later use an approach to avoid the energy ratio being maximized at the m' th tap. For now, we just assume that the ToA estimate is $\bar{\tau}_m$ and analyze $\gamma_n(\bar{\tau}_1)$ at the m th tap.

Estimate ToA with $\bar{\tau}_m$

From Proposition 6, we know that $|\bar{h}_m(\bar{\tau}_1, 1)|$ is a decreasing function of $|\tau_1 - \bar{\tau}_m|$. Similarly, $|\bar{h}_m(\bar{\tau}_1, 2)|$ and $|\bar{h}_{m-1}(\bar{\tau}_1, 2)|$ which are the energy captured from the second path are increasing functions of $|\tau_2 - \bar{\tau}_{m'}|$. Due to the relationship $\tau_2 = (p + 0.5)T_p + \tau_1$, $|\tau_2 - \bar{\tau}_{m'}|$ decreases as $|\tau_1 - \bar{\tau}_m|$ increases. For these reasons, both $|\bar{h}_m(\bar{\tau}_1, 2)|$ and $|\bar{h}_{m-1}(\bar{\tau}_1, 2)|$ are increasing functions of $|\bar{h}_m(\bar{\tau}_1, 1)|$. From (36), the maximum value of $|\bar{h}_m(\bar{\tau}_1, 1)|$ is h_1 when the first path is exactly sampled. When $\bar{\tau}_m = (\tau_1 - 0.5T_p)$, $|\bar{h}_m(\bar{\tau}_1, 1)|$ reaches its minimum value

$$|\bar{h}_m(\bar{\tau}_1, 1)| = \left| \frac{h_1}{N} \cdot \frac{\sin(0.5\pi)}{\sin(0.5\pi/N)} \right| \approx \frac{2h_1}{\pi}. \quad (42)$$

In order to relate $|\bar{h}_m(\bar{\tau}_1, 1)|$ with $|\bar{h}_m(\bar{\tau}_1, 2)|$ and $|\bar{h}_{m-1}(\bar{\tau}_1, 2)|$, we use the following approximation

$$\begin{aligned} |\bar{h}_n(\bar{\tau}_1, 2)|^2 &= \left(|\bar{h}_m(\bar{\tau}_1, 1)| - \frac{2h_1}{\pi} \right)^2 c_e(n), \\ n &= m, m-1, |\bar{h}_m(\bar{\tau}_1, 1)| \in [2h_1/\pi, h_1] \end{aligned} \quad (43)$$

where $2h_1/\pi$ is the minimum value of $|\bar{h}_m(\bar{\tau}_1, 1)|$. Coefficients $\{c_e(n)\}_{n=m-1}^m$ reflect the interference strength from the second path. In particular, the stronger the second path or the smaller the inter-path interval, the larger $\{c_e(n)\}_{n=m-1}^m$. Numerical analysis shows that $c_e(n)$ is almost independent with $|\tau_1 - \bar{\tau}_m|$. Therefore, $c_e(n)$ can be approximated to be constant to $|\tau_1 - \bar{\tau}_m|$ and accordingly to $|\bar{h}_m(\bar{\tau}_1, 1)|$. In addition, numerical result shows that $c_e(m-1) \approx c_e(m)$ which especially holds when the inter-path interval is large.

From Proposition 6, $|\bar{h}_{m-1}(\bar{\tau}_1, 1)|$ decreases as $|\bar{h}_m(\bar{\tau}_1, 1)|$ increases. Based on this, we use the approximation $|\bar{h}_{m-1}(\bar{\tau}_1, 1)|^2 \approx h_1^2 - |\bar{h}_m(\bar{\tau}_1, 1)|^2$. Then, the energy ratio at the m th tap of

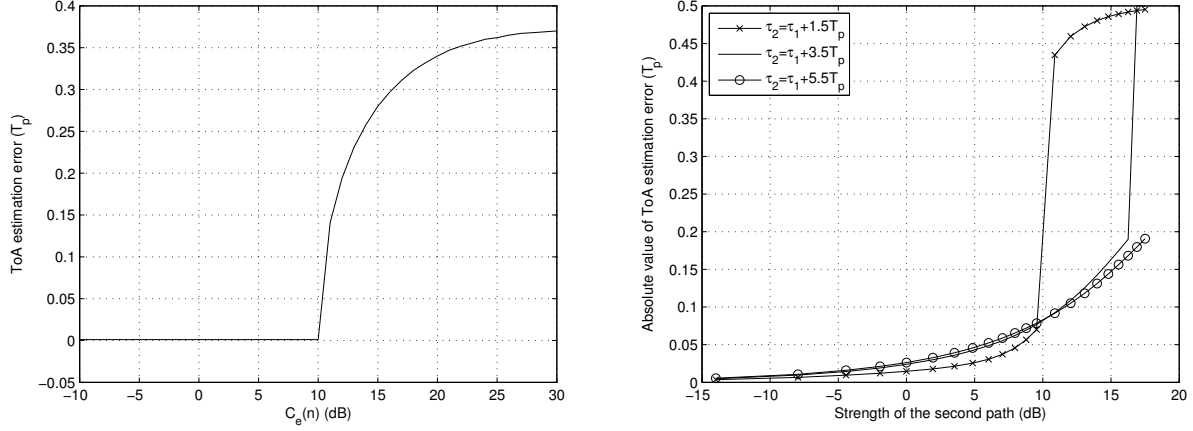


Figure 6: (a) ToA estimation by the maximizing Eq. (44). (b) ToA estimation by maximizing the energy ratio at the strongest component tap of the first path; two path channel.

the estimated channel (41) is simplified as

$$\gamma_m(\bar{\tau}_1) \approx \frac{|\bar{h}_m(\bar{\tau}_1, 1)|^2 + (|\bar{h}_m(\bar{\tau}_1, 1)| - 2h_1/\pi)^2 c_e(m)}{h_1^2 - |\bar{h}_m(\bar{\tau}_1, 1)|^2 + (|\bar{h}_m(\bar{\tau}_1, 1)| - 2h_1/\pi)^2 c_e(m)}, \quad (44)$$

$$|\bar{h}_m(\bar{\tau}_1, 1)| \in [2h_1/\pi, h_1].$$

Eq. (44) contains a single independent variable $|\bar{h}_m(\bar{\tau}_1, 1)|$ with the coefficient $c_e(m)$ modeling the interference from the second path. For each $c_e(m)$, the ToA estimate can be calculated by searching $|\bar{h}_m(\bar{\tau}_1, 1)|$ to maximize the energy ratio (44). Fig. 6(a) shows that the ToA estimation error decreases as $c_e(m)$ decreases, which is a quite reasonable result. In addition, when $c_e(m)$ is very small, the ToA estimation is always accurate. When $c_e(m)$ is large, the ToA estimation error will rapidly increase because the second path is dominant.

Fig. 6(b) shows the numerical result for the two-path channel where the ToA is estimated by maximizing the energy ratio of (39) at the m th tap that contains the strongest contribution from the first path. As predicted by the approximate analysis in Eq. (44), the ToA estimation error decreases either as the inter-path interval increases or the second path strength decreases, both of which result in a smaller $c_e(m)$. When the inter-path interval is large, the ToA estimate is very accurate since inference from the second path is very weak. As the second path strength increases, the ToA estimation error will rapidly increase since the inter-path inference becomes dominant.

Avoid the Fake ToA Estimate $\bar{\tau}_{m'}$

In the preceding analysis, we estimate the ToA by searching $\bar{\tau}_1$ to maximize the energy

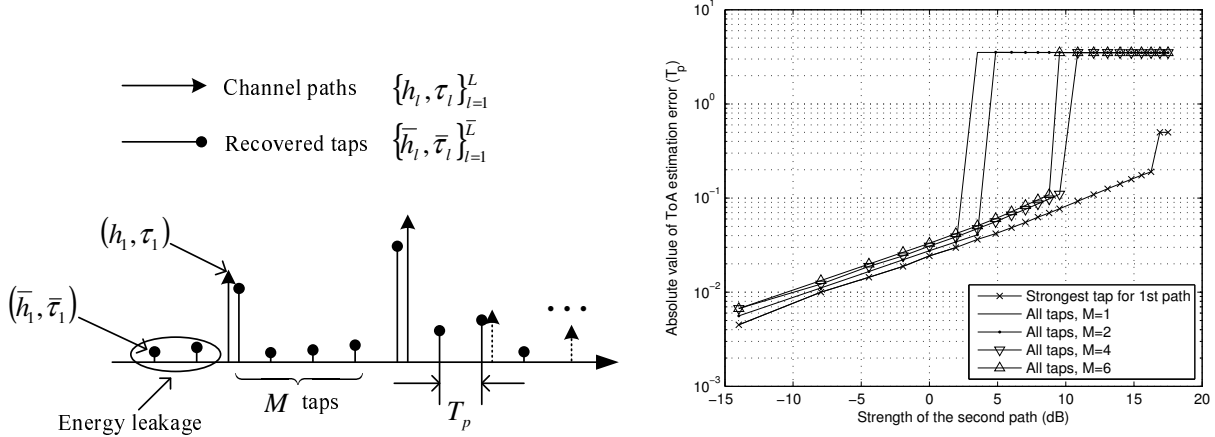


Figure 7: (a) Avoid picking out the second path; $M = 4$. (b) ToA estimation by maximizing the energy ratio among the reconstructed taps for the two path channel; $\tau_2 = \tau_1 + 3.5T_p$.

ratio $\gamma_n(\bar{\tau}_1)$ at the m th tap that contains the strongest contribution from the first path. For this approach to be realistic, we need to avoid the energy ratio $\gamma_n(\bar{\tau}_1)$ being maximized at the m' th tap that contains the strongest contribution from the second path. We use the following modified energy ratio

$$\gamma_n(\bar{\tau}_1, M) = \frac{|\bar{h}_n(\bar{\tau}_1)|^2}{\frac{1}{M} \sum_{i=n-M}^{n-1} |\bar{h}_i(\bar{\tau}_1)|^2}, \quad n \in [L_1, L_2]. \quad (45)$$

Different from (41), the denominator in (45) also includes $(M - 1)$ taps prior to the current tap. Therefore, if M is sufficiently large, denominator of the m' th tap will not only include the weak energy leakage of both paths but also the strong energy leakage from the first path (see Fig. 7(a)). In comparison, denominator of the m th tap only contains weak energy leakage from both paths. As a result, it will be less likely for Eq. (45) to reach its maximum value at taps that contain strong energy from the second path.

The validity of this method has been confirmed by the numerical analysis where the ToA is estimated by searching for the maximum value of $\gamma_n(\bar{\tau}_1, M)$ among all taps of the estimated channel (see Fig. 7(b)). In Fig. 7(b), an optimal value of M exists that optimizes the ToA estimation performance. When M is smaller than this value, ToA estimation accuracy improves as M increases since it becomes less likely to pick out the trailing paths when more leading paths are included in the denominator of $\gamma_n(\bar{\tau}_1, M)$. As M continuously increases, ToA estimation performance will again degrade. This is because as more weaker energy

leakage taps prior to the first path are included, the estimator becomes less sensitive to the ToA estimation error. Simulations show that these results also hold for the IEEE 802.15.4a UWB channels.

D.3.2 ToA Estimation for Multipath Channels

Based on the preceding discussions, we have the following ToA estimation algorithm for general multipath channels.

Proposed Algorithm: For each $\bar{\tau}_1 \in [0, T_p)$, we evaluate the energy ratio $\gamma_n(\bar{\tau}_1, M) = |\bar{h}_n(\bar{\tau}_1)|^2 / (\frac{1}{M} \sum_{i=n-1}^{n-M} |\bar{h}_i(\bar{\tau}_1)|^2)$ at the n th tap, $n \in [L_1, L_2]$. $[L_1, L_2]$ represents the remaining ToA estimation error after the coarse timing. Then find the $(\bar{\tau}_1, n)$ pair that maximizes the energy ratio $\gamma_n(\bar{\tau}_1, M)$:

$$(\hat{\tau}_1, \hat{n}) = \underset{0 \leq \bar{\tau}_1 < T_p, L_1 \leq n \leq L_2}{\operatorname{argmax}} \gamma_n(\bar{\tau}_1, M). \quad (46)$$

The ToA estimate can then be obtained as:

$$\hat{\tau}_1 = \hat{\tau}_1 + (\hat{n} - 1)T_p. \quad (47)$$

The range of $\bar{\tau}_1$ in (46) has been reduced to $[0, T_p)$ as compared to the $[0, T_h]$ in Eq. (38) where T_h is the maximum channel delay spread. This is because for the equally-spaced model, the energy ratio satisfies $\gamma_n(\bar{\tau}_1 + kT_p, M) = \gamma_{n+k}(\bar{\tau}_1, M)$ for $\bar{\tau}_1 \in [0, T_p)$ with k being an integer (see (36)). Therefore, it is sufficient to limit $\bar{\tau}_1$ in $[0, T_p)$ when $\gamma_n(\bar{\tau}_1, M)$ is also maximized with respect to the tap index.

D.3.3 FoFa versus Traditional ToA Estimators

When the model-based channel estimator is used for ToA estimation, it can not achieve the best accuracy provided by the channel condition. As FoFa, the model-based estimator also uses (33) to estimate the channel. However, it does not consider the optimal choice of $\bar{\tau}_1$ in the sense of ToA estimation. From Fig. 5(a), we can see that with a bad choice of $\bar{\tau}_1$, delay of any of the first 5 taps could be used as the ToA estimate, due to their sufficiently large amplitudes. In such cases, the resulting ToA estimation error will be comparable to, or even much greater than, the tap spacing. Actually, with an intention to solve this problem, the FoFa ToA estimator can be regarded as an enhanced sample-spaced estimator.

As introduced previously, all computations in the FoFa ToA estimator are performed in baseband which avoids the manipulation of analog waveforms as in correlator-based esti-

mators. In addition, FoFa uses the channel frequency response coefficients for ToA estimation which are already available for equalization purposes in FDE systems such as OFDM and SC-FDE. Therefore, the FoFa ToA estimator can achieve a much lower hardware cost by building on existing FDE structures with minimum alteration.

Traditionally, ToA estimation can also be carried out via channel estimation which aims at maximizing the likelihood or minimizing the error between the estimates of all paths and the true ones. Since the contribution from the first path is small, these estimators often encounter poor convergence or suffer from local optimum problems when being used as ToA estimators. The FoFa ToA estimator directly addresses the delay estimation of the first channel path. Therefore, FoFa can outperform the traditional channel-estimation-based ToA estimators in terms of accuracy. This can be verified by simulations for FoFa and the well-known SAGE algorithm. Furthermore, the FoFa ToA estimator is computationally efficient since we focus on the estimation of a single parameter.

D.4 Summary

In this research, we propose a high-precision ToA estimator by *focusing on the first arrival* (FoFa). The ToA estimator relies on a novel criterion; that is, locating the first channel path by minimizing the energy leakage prior to the first path. By directly addressing the estimation of the first channel path, the proposed ToA estimator can outperform the traditional SAGE algorithm in terms of accuracy and computational efficiency. Furthermore, the proposed ToA estimator operates in baseband to avoid the complicated manipulation of the analog or oversampled waveform at the receiver, and can be implemented with minimum alteration of existing FDEs.

E Ranging with Multi-Band UWB Signals: Coherent vs. Non-coherent Combination

In our approach, the tap spacing T_p dictates the resolution of the candidate set $\{\bar{h}_l, \bar{\tau}_l\}_{l=1}^{\bar{L}}$. At the first glance, it appears that the timing resolution can be arbitrarily improved by reducing T_p . However, when T_p is smaller than the inverse of the bandwidth occupied by the channel frequency response coefficients, the matrix $\mathbf{G}^H(\bar{\tau}_1)\mathbf{G}(\bar{\tau}_1)$ in (33) tends to be ill-conditioned

and the problem becomes unsolvable. This is because, even though the Vandermonde matrix $\mathbf{G}(\bar{\tau}_1)$ always has full column rank, columns of $\mathbf{G}(\bar{\tau}_1)$ become increasingly correlated as T_p decreases. In the extreme case when $T_p \rightarrow 0$, the rank of $\mathbf{G}(\bar{\tau}_1)$ becomes one. For this reason, the achievable resolution of the estimator is constrained by the used bandwidth. This bandwidth versus resolution problem has also been mentioned in the literature in a different context.

For multi-band systems such as the MB-OFDM UWB, two strategies can be adopted to combine the channel information from subbands: the *coherent combining* and the *noncoherent combining*. For the coherent combining, estimates of channel frequency response coefficients for all subbands are jointly used to estimate the time domain channel with Eq. (33). For the noncoherent combining, the time domain channel is first estimated for each subband. Then, the ToA estimates obtained from all subbands are averaged for a better final estimate. The bandwidth used by the coherent combining is larger than each individual subband. In addition, the smallest model resolution T_p is the inverse of the bandwidth that is used for the time domain channel estimation. The coherent combining can provide a better resolution than the noncoherent combining.

It should be noted that, as other ToA estimation techniques in the literature, the coherent combining in the FoFa ToA estimator also requires that no random phase rotation exists in subband signals after carrier demodulation. If there is random phase rotation, one would have to adopt the noncoherent combining. In addition, the resolution enhancement by the coherent combining is obtained at the price of increased computational complexity by computing the inverse of $\mathbf{G}^H(\bar{\tau}_1)\mathbf{G}(\bar{\tau}_1)$ of a greater dimension.

We simulate the performance of the FoFa ToA estimator based on the UWB MB-OFDM system specified in the ECMA-368 standard. In this standard, the entire UWB spectrum is divided into 14 equally-sized subbands. For each subband with a bandwidth of 528 MHz, the multicarrier modulation/demodulation is performed with a 128 point IFFT/FFT. A total of 122 subcarriers are used as data, guard and pilot subcarriers. Each simulation is carried out in 2000 randomly generated channel realizations. As the performance of the subspace-based algorithms are usually quite sensitive to channel order mismatch, we will only compare the performance of the FoFa ToA estimator with the SAGE algorithm.

We first compare FoFa with the SAGE algorithm in the IEEE 802.15.4a LoS office channel (CM3) (see Fig. 9(a)). Assume that the remaining timing ambiguity is ± 4.5 ns after the coarse synchronization. The M in (45) is set so that the average energy is calculated in the

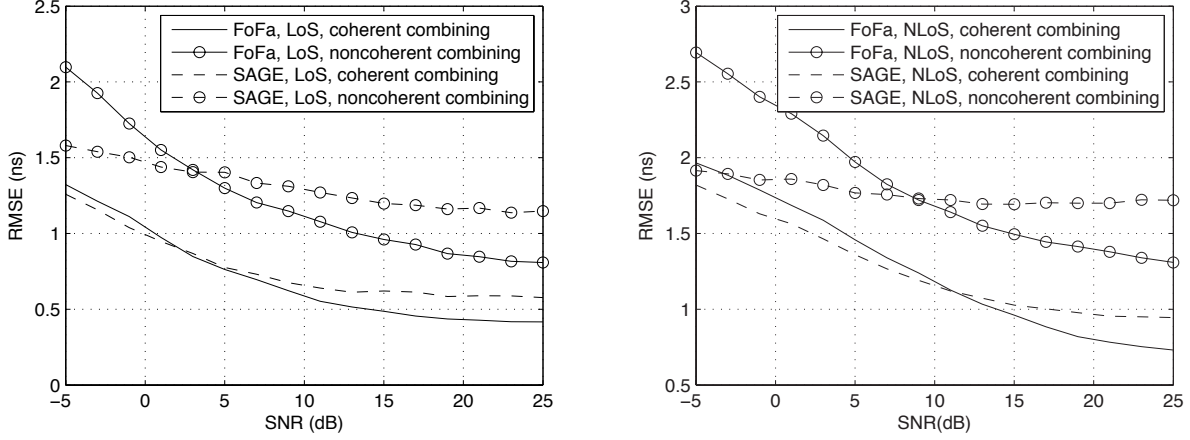


Figure 8: (a) The RMSE performance of SAGE and the FoFa ToA estimator in LoS channels. (b) The RMSE performance of SAGE and the FoFa ToA estimator in NLoS channels.

range of 2 ns. For a fair comparison, the channel estimates obtained by using Eq. (33) with a random $\bar{\tau}_1$ are fed to the SAGE ToA estimator as the initial state of the iterative algorithm.

Fig. 9(a) shows the root-mean-square error (RMSE) performance of FoFa and SAGE when the 3 subbands are either coherently or noncoherently combined. For both estimators, the RMSE is much smaller than the receiver sampling interval 1.89 ns=1/528 MHz at high SNR. For both coherent and noncoherent combining, SAGE outperforms the FoFa estimator at low SNR. This is because the SAGE algorithm estimates the delays and amplitudes of all channel paths. At high SNR, FoFa outperforms SAGE by directly estimating the ToA. With our setup, the Matlab simulation time of the SAGE estimator is about 10 times that of FoFa¹. Although the simulation codes are not optimized, this can somehow show that the FoFa ToA estimator is more computationally efficient. In Fig. 9(a), we also compare the performance of both coherent combining and noncoherent combining. As predicted in the preceding analysis, the coherent combining shows a better resolution (high SNR performance) than the noncoherent combining due to the improved resolution of $\{\bar{h}_l, \bar{\tau}_l\}_{l=1}^L$.

The FoFa and SAGE ToA estimators are then evaluated and compared in the IEEE 802.15.4a non-line-of-sight (NLoS) office channel (CM4) (see Fig. 9(b)). Compared to the LoS channel environment, both estimators show performance degradations. Notice that this is also a common problem for existing timing and synchronization algorithms, because in the NLoS scenario, the first channel path is not necessary to be a strong one and the synchronization

¹For SAGE, we have used the time of one iteration for comparison.

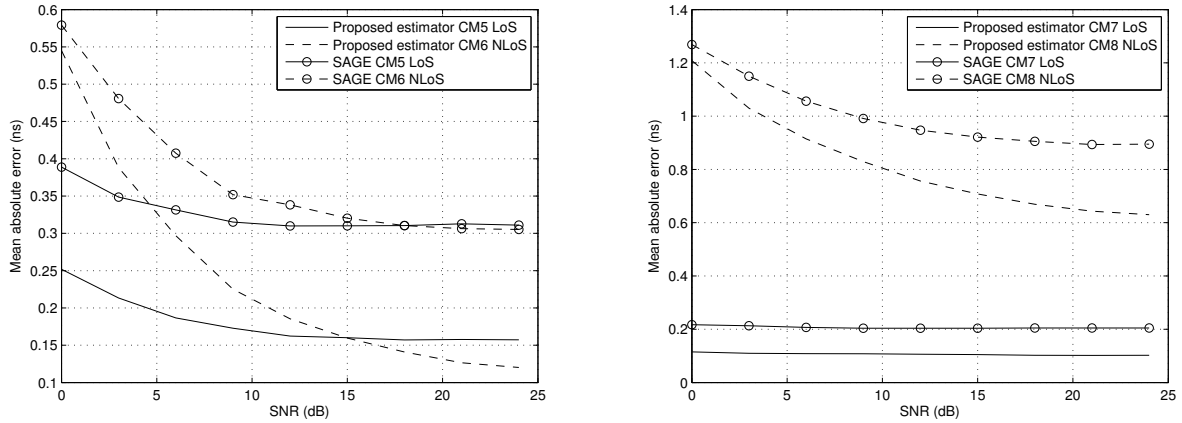


Figure 9: (a) ToA estimation for the outdoor LoS and NLoS channels. (b) ToA estimation for the industrial LoS and NLoS channels.

is more likely to be affected by noise and the trailing paths.

We further test our algorithm in outdoor and industrial UWB channels. Figs. 9(a) and 9(b) show that performance in LoS channels is better than the corresponding NLoS channels. This is because in the NLoS channel, the first path may not be strong and the estimator is more affected by the trailing paths. However, there is an exception for the outdoor environment at high SNR. Comparing their channel realizations, we find that channel paths in CM6 are weaker but sparser than CM5. As a result, the CM6 channel can be better resolved than CM5 and the localization of its first path will be less interfered by its trailing paths.

The proposed ToA estimator is also compared with the SAGE-based ToA estimator. Channel estimate results obtained by (33) with a random $\bar{\tau}_1$ are fed to the SAGE-based ToA estimator as the initial state of the iterative algorithm. Simulations show that FoFa outperforms SAGE. SAGE is a practical method to estimate multiple parameters due to its fast convergence than the EM algorithm. However, SAGE has the local optimum problem, especially when the number of unknown parameters is large. Therefore, the estimated channel may not be very close to the real channel at the first path. The proposed ToA estimator directly estimates the first path delay, without unnecessarily caring about the estimation errors for the trailing paths and therefore enables a better ToA estimation performance.

F Ranging with Multi-Band UWB Signals: Random Phase Rotation

Multi-band orthogonal frequency-division multiplexing (MB-OFDM) UWB systems combine OFDM and frequency hopping that periodically alters the carrier frequency among multiple subbands. Due to their huge bandwidth, UWB systems can realize high resolution time-of-arrival (TOA) estimation for time-based wireless ranging and localization. For MB-OFDM, this capability can be further enhanced if channel information is collected from multiple subbands to estimate the TOA.

TOA estimation is usually carried out in two steps. First, the time domain channel is estimated. Then, the first path is detected from the channel estimate and its delay is used as the TOA estimate. In order to achieve high resolution channel estimation, channel information from multiple subbands should be coherently combined so that consecutive subbands are treated as a single larger band. Coherent combining requires that subband signals have the same phase rotation after carrier demodulation. However, this cannot be guaranteed by MB-OFDM receivers due to the uncertain initial phase states of modulator and demodulator oscillators. Therefore, it is necessary to develop a signal processing algorithm to calibrate random phase rotations across subbands.

The proposed phase rotation calibration algorithm relies on the energy leakage phenomenon which has been used for precise TOA estimation as discussed in the preceding section. Energy leakage is essentially due to the limited resolution of finite signal bandwidth when the channel is estimated. Analysis in this work indicates that in the presence of random phase rotations, resolution of MB-OFDM signals degrades which is reflected by increased energy leakage in the channel estimate. Based on this, we propose to calibrate phase rotations of subbands by suppressing the energy leakage effect. Validity of the proposed technique is corroborated in IEEE 802.15.4a UWB channels.

F.1 MB-OFDM System Model

At the MB-OFDM transmitter (see Fig. 10(a)), information bits are mapped to constellation points and multi-carrier modulated by inverse fast Fourier transform (IFFT). In order to avoid the inter-symbol interference (ISI), guard interval (GI) is added to each OFDM symbol. After digital-to-analog conversion (DAC), baseband signals are carrier modulated and

transmitted from antenna. At the receiver (see Fig. 10(b)), received signals are carrier demodulated and analog-to-digital converted (ADC). After coarse timing, GI is removed and the baseband signals are multi-carrier demodulated by FFT.

MB-OFDM systems can periodically alter the carrier frequency according to the time-frequency code known to both transmitter and receiver (see Fig. 11). Due to the uncertain phases of transmitter and receiver oscillators (ϕ_t and ϕ_r in Fig. 10), baseband received signals contain a random phase rotation $\bar{\phi} = (\phi_t - \phi_r)$ which varies in the range between 0 and 2π . Although the random phase rotation can even change when the system twice enters the same subband, we mainly focus on the inter-band phase calibration across different subbands. After that, we will briefly introduce how to perform the intra-band phase calibration.

Same as the single-band OFDM, MB-OFDM can convert the frequency selective channel to parallel flat fading channels, each corresponding to a subcarrier. Suppose that the system operates over B subbands and each subband contains K subcarriers. The received signal $r_{b,k}$ on the k th ($0 \leq k \leq K-1$) subcarrier of the b th ($0 \leq b \leq B-1$) subband can be expressed as:

$$r_{b,k} = s_{b,k}H_{b,k}\exp(j\bar{\phi}_b) + \xi_{b,k} . \quad (48)$$

In Eq. (48), $s_{b,k}$ is the signal transmitted on the k th subcarrier of the b th subband and $\xi_{b,k}$ is noise. $H_{k,b}$ is the channel Fourier transform coefficient:

$$H_{b,k} = \sum_{l=0}^{L-1} h_l \exp(-j\omega_{b,k}\tau_l) \quad (49)$$

where $\{h_l\}_{l=0}^{L-1}$ and $\{\tau_l\}_{l=0}^{L-1}$ are multipath amplitudes and delays of the channel impulse response (CIR)

$$h(t) = \sum_{l=0}^{L-1} h_l \delta(t - \tau_l) , \quad (50)$$

and $\omega_{b,k}$ is the frequency of the (k, b) th subcarrier. $\bar{\phi}_b$ is the random phase rotation in baseband signals of the b th subband.

Based on (48), channel information can be obtained in frequency domain by the following operation:

$$\bar{H}_{b,k} = \frac{r_{b,k}}{s_{b,k}} = H_{b,k}\exp(j\bar{\phi}_b) + \eta_{b,k} \quad (51)$$

where $\eta_{b,k} = \xi_{b,k}/s_{b,k}$ is noise.

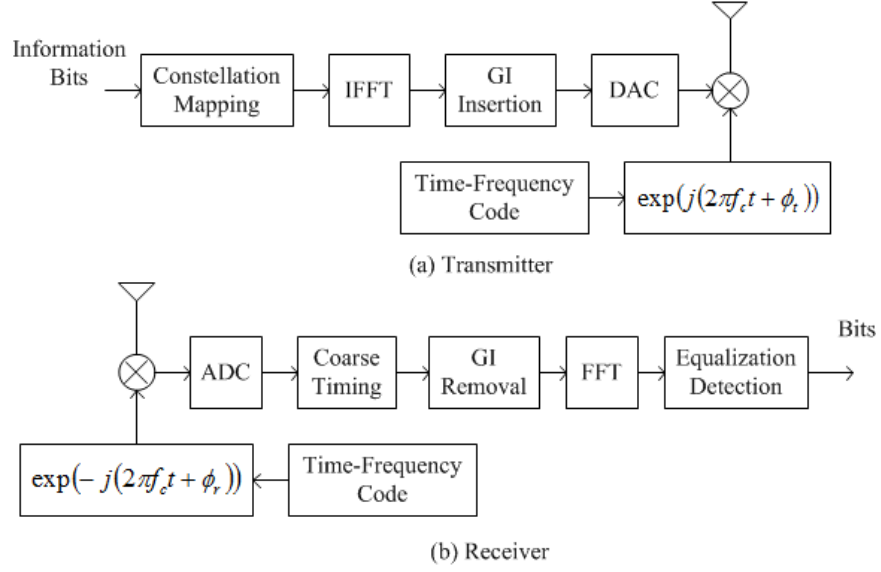


Figure 10: MB-OFDM system model.

F.2 Channel Estimation with Coherent Combining

The random phase rotation problem is encountered in channel estimation with coherent combining which is the first step of high resolution TOA estimation for MB-OFDM. In the absence of *a priori* channel information, the maximum likelihood (ML) criterion results in the optimal channel estimator. Given that $\xi_{b,k}$ in Eq. (48) is white Gaussian, the ML channel estimator obtains estimates of $\{h_l\}_{l=0}^{L-1}$, $\{\tau_l\}_{l=0}^{L-1}$ and nuisance parameters $\{\bar{\phi}_b\}_{b=0}^{B-1}$ when the following squared error

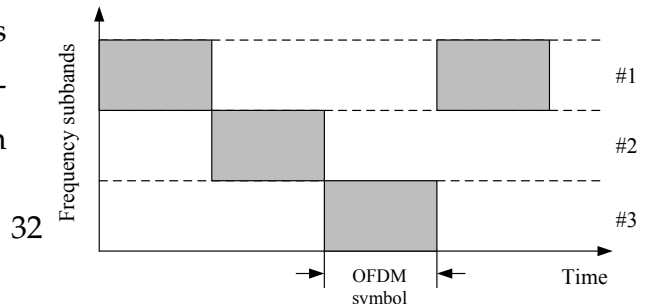
$$\mathbf{E} = \sum_{b=0}^{B-1} \sum_{k=0}^{K-1} |r_{b,k} - \hat{r}_{b,k}|^2 \quad (52)$$

is minimized between received signals and their reconstructed versions

$$\hat{r}_{b,k} = s_{b,k} \sum_{l=0}^{L-1} \hat{h}_l \exp(-j\omega_{b,k} \hat{\tau}_l) \exp(j\hat{\phi}_b) . \quad (53)$$

The ML estimator is too computationally intensive to be feasible for UWB channels due to the huge number of multipath components.

In order to maintain low complexity, many channel estimation related problems are investigated based on the sampled channel. This suggests that the time domain



channel can be reconstructed by fitting frequency domain channel information (51) to the following sequence with equally-spaced samples:

$$\bar{h}(t) = \sum_{n=0}^{\bar{L}-1} \bar{h}_n \delta(t - \bar{\tau}_n). \quad (54)$$

The sequence $\bar{h}(t)$ contains \bar{L} samples with amplitudes $\{\bar{h}_n\}_{n=0}^{\bar{L}-1}$ and delays $\{\bar{\tau}_n\}_{n=0}^{\bar{L}-1}$. Given the first sample delay $\bar{\tau}_0$ and sample spacing T_p , delays of other samples can be determined as $\bar{\tau}_n = \bar{\tau}_0 + nT_p$, $1 \leq n \leq \bar{L} - 1$. In order to reconstruct the whole CIR, $\bar{L}T_p$ should be larger than the maximum channel delay spread. In this work, tap spacing T_p is chosen as the inverse of the entire bandwidth of all subbands which is known as the system resolution. Compared to the ML criterion (52) and (53), this estimator has much lower-complexity because it has only one free parameter $\bar{\tau}_0$. In the preceding section, $\bar{\tau}_0$ is optimized for TOA estimation when the mistiming induced energy leakage is minimized.

For each arbitrary $\bar{\tau}_0$, sample amplitudes of sequence (54) can be obtained by fitting $\{\bar{h}_n\}_{n=0}^{\bar{L}-1}$ to the frequency domain channel information (51) as

$$\sum_{n=0}^{\bar{L}-1} \bar{h}_n \exp(-j\omega_{b,k} \bar{\tau}_n) = \bar{H}_{b,k}, \quad (55)$$

$$0 \leq k \leq K - 1, 0 \leq b \leq B - 1$$

As all subbands have been incorporated into channel estimation, Eq. (55) results in a coherent combining of MB channel information.

The relationship (55) can be expressed in matrix form as

$$\mathbf{G}\bar{\mathbf{h}} = \bar{\mathbf{H}} \quad (56)$$

where $\bar{\mathbf{H}} = [\bar{H}_{0,0}, \bar{H}_{0,1}, \dots, \bar{H}_{B-1,K-1}]^T$ contains all frequency domain channel information, $\bar{\mathbf{h}} = [\bar{h}_0, \bar{h}_1, \dots, \bar{h}_{\bar{L}-1}]^T$ is the vector of sample amplitudes and \mathbf{G} is the Fourier transform matrix determined by Eq. (55). A simple least squares (LS) solution of (56) can be formed as

$$\bar{\mathbf{h}} = (\mathbf{G}^H \mathbf{G})^{-1} \mathbf{G}^H \bar{\mathbf{H}}. \quad (57)$$

It should be noted that $\bar{\mathbf{h}}$ depends on the first sample delay $\bar{\tau}_0$ through \mathbf{G} .

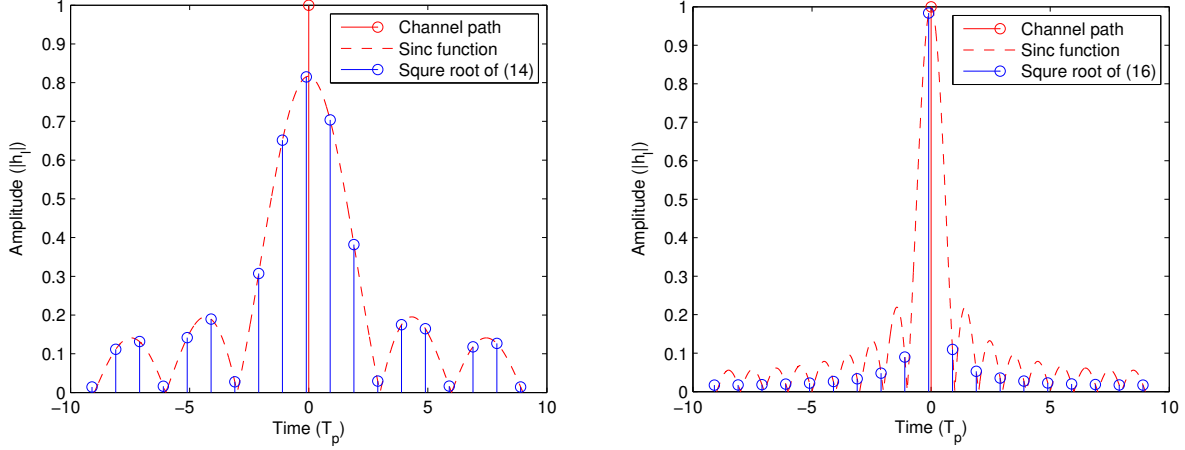


Figure 12: (a) Amplitude of the l th path's information in the estimated channel in the presence of random phase rotations. (b) Amplitude of the l th path's information in the estimated channel in the absence of random phase rotations.

As mentioned above, sample spacing T_p is chosen to be the inverse of the entire bandwidth. There are two reasons for this. First, if T_p is smaller than this value, $\mathbf{G}^H \mathbf{G}$ in Eq. (57) tends to be ill-conditioned and the problem becomes unsolvable. Secondly, given this T_p , $\mathbf{G}^H \mathbf{G}$ is an identity matrix and the computational cost is reduced by avoiding calculating $(\mathbf{G}^H \mathbf{G})^{-1}$.

E.3 Analysis and Calibration of Random Phase Rotation Effect

In this section, we first analyze the impact of random phase rotations to channel estimation. Based on the analysis result, we will propose our random phase rotation calibration algorithm.

E.3.1 With Random Phase Rotations

Because Eqs. (49) and (55) are linear to the L channel multipath components, the n th sample \bar{h}_n of the estimated channel $\bar{h}(t)$ is the superposition of information obtained from all L paths

$$\bar{h}_n = \sum_{l=0}^{L-1} \bar{h}_n(l) + \bar{\eta}_n, 0 \leq n \leq \bar{L} - 1. \quad (58)$$

In Eq. (58), $\bar{\eta}_n$ is the noise term and $\bar{h}_n(l)$ contains channel information obtained from the l th multipath component which can be expressed by

$$\bar{h}_n(l) = h_l \sum_{b=0}^{B-1} \exp(j\bar{\phi}_b) \exp\left(j\frac{2\pi b}{BT_p}(\bar{\tau}_n - \tau_l)\right) \times \bar{h}_n^s(l) \quad (59)$$

and

$$\bar{h}_n^s(l) = \exp\left(\frac{j\pi(K-1)(\bar{\tau}_n - \tau_l)}{NT_p}\right) \times \frac{\sin(\pi(\bar{\tau}_n - \tau_l)/(BT_p))}{N \sin(\pi(\bar{\tau}_n - \tau_l)/(NT_p))}. \quad (60)$$

In Eq. (59), $\bar{h}_n(l)$ contains channel information collected from all B subbands distorted by random phase terms $\{\exp(j\bar{\phi}_b)\}_{b=0}^{B-1}$ with $\{\bar{\phi}_b\}_{b=0}^{B-1}$ being uniformly distributed in the range between 0 and 2π . Energy captured by $\bar{h}_n(l)$ is random but its mean value can be obtained as (cf. (59)):

$$\mathbb{E}\left(|\bar{h}_n(l)|^2\right) = h_l^2 \frac{\sin^2(\pi(\bar{\tau}_n - \tau_l)/(BT_p))}{KN \sin^2(\pi(\bar{\tau}_n - \tau_l)/(NT_p))}. \quad (61)$$

Note that the energy in Eq. (61) is determined by the discrete sinc function sampled at time instants $(\bar{\tau}_n - \tau_l), 0 \leq n \leq \bar{L} - 1$.

Fig. 12(a) shows an example of Eq. (61) where the blue line represents the l th channel path with delay $\tau_l = 0$ and red lines are square root of Eq. (61) with their envelope (dashed line) being the discrete sinc function. The sinc function has a main lobe width of $2BT_p$. From the definition of T_p , BT_p is the inverse of bandwidth of a single subband. This implies that no matter how many subbands are used, in the presence of random phase rotations, resolution of channel estimation is only facilitated by subband bandwidth. As shown in Fig. 12(a), even for a single channel path, multiple samples in the estimated channel contain non-zero energy. This is known as the energy leakage phenomenon. It should be noted that due to the random phase rotation effect, energy leakage cannot be avoided by horizontally shifting the sequence (see Fig. 12(a)).

E.3.2 Without Random Phase Rotations

In this case, we assume that phase rotations of all subbands have been perfectly calibrated to the same value, for example $\bar{\phi}_0$. Then information of the l th path in the estimated channel

can be expressed as (cf. (59))

$$\begin{aligned} \bar{h}_n(l) = & h_l \exp(j\bar{\phi}_0) \exp\left(\frac{j\pi(N-1)(\bar{\tau}_n - \tau_l)}{NT_p}\right) \\ & \times \frac{\sin(\pi(\bar{\tau}_n - \tau_l)/T_p)}{N \sin(\pi(\bar{\tau}_n - \tau_l)/(NT_p))}. \end{aligned} \quad (62)$$

Energy captured by the n th sample from the l th channel path is also a sampled discrete sinc function but with a smaller main lobe width of $2T_p$ (see Fig. 12(b)):

$$|\bar{h}_n(l)|^2 = h_l^2 \frac{\sin^2(\pi(\bar{\tau}_n - \tau_l)/T_p)}{N^2 \sin^2(\pi(\bar{\tau}_n - \tau_l)/(NT_p))}. \quad (63)$$

Same as (61), Eq. (63) still shows energy leakage dispersed from the l th path over $\{\bar{h}_n(l)\}_{n=0}^{\bar{L}-1}$. However, when the l th path is exactly sampled by the sequence if a proper $\bar{\tau}_0 \in [0, T_p)$ is chosen, energy leakage in Eq. (63) vanishes and all energy of the l th path is captured by the sample that has delay of τ_l . This is not a property possessed by (61) when random phase rotations exist.

The difference between (61) and (63) indicates that energy leakage can be induced by not only missampling but also the random phase rotation effect. In the presence of random phase rotations, main lobe of (61) is B times wider than (63) which results in a more dispersive energy leakage. These suggest that $\{\bar{\phi}_b\}_{b=0}^{B-1}$ can be calibrated by suppressing the additional energy leakage induced by random phase rotations.

E.3.3 Phase Rotation Calibration Algorithm

Fig. 5(a) shows the real-valued UWB channel and amplitude of the channel estimate (58) using the first two subbands of the ECMA-368 MB-OFDM system. For multipath channels with continuously varying delays, energy leakage always exists because the equally-spaced sequence cannot exactly sample all channel paths. Among all samples in the channel estimate, those prior to the first channel path can well reflect the extent of energy leakage because no multipaths fall in this range. We have seen that, TOA is estimated by choosing a proper $\bar{\tau}_0$ so that the missampling induced energy leakage contained by these samples is minimized. For phase rotation calibration, energy leakage is induced by both missampling and random phase rotations. Therefore, energy leakage prior to the first path can be minimized by choosing proper values for both $\bar{\tau}_0$ and $\{\bar{\phi}_b\}_0^{B-1}$. Based on this, random phase rotations can be calibrated across subbands by the following algorithm.

Proposed Algorithm: After coarse timing, select M samples $\{\bar{h}_n\}_{n=0}^{M-1}$ before the first channel path that only contain energy leakage. For each $\bar{\tau}_0 \in [0, T_p)$ and $\bar{\phi}_b \in [0, 2\pi)$, $b \in [1, B - 1]$, calculate the total energy leakage of these M samples

$$\mathcal{E}(\bar{\tau}_0, \{\bar{\phi}_b\}_{b=1}^{B-1}) = \sum_{n=0}^{M-1} |\bar{h}_n|^2. \quad (64)$$

Then find $\bar{\tau}_0$ and $\{\bar{\phi}_b\}_{b=1}^{B-1}$ that minimize the energy leakage

$$(\hat{\tau}_0, \{\hat{\phi}_b\}_{b=1}^{B-1}) = \underset{0 \leq \bar{\tau}_0 < T_p, 0 \leq \bar{\phi}_b < 2\pi}{\operatorname{argmin}} \mathcal{E}(\bar{\tau}_0, \{\bar{\phi}_b\}_{b=1}^{B-1}). \quad (65)$$

Correct phase rotations by multiplying the b th subband's received signals with $\exp(-j\hat{\phi}_b)$.

F.3.4 Discussions

We have introduced the inter-band phase calibration of different subbands. It should be noted that phase rotation also changes when the system twice enters the same subband. Suppose that $\bar{\phi}_b(i)$ and $\bar{\phi}_b(i+1)$ are phase rotations when the system for the i th and $(i+1)$ th times enters the b th subband and channel does not change in this period. Calibration of $\bar{\phi}_b(i)$ and $\bar{\phi}_b(i+1)$ can be simply realized by using the phase of the following correlation:

$$\mathcal{R}(i, i+1) = \sum_{k=1}^K r_{b,k}(i)r_{b,k}^*(i+1). \quad (66)$$

In Eq. (66), the same set of training data $\{s_{b,k}\}_{k=0}^{K-1}$ are transmitted for received signals $\{r_{b,k}(i)\}_{k=0}^{K-1}$ and $\{r_{b,k}(i+1)\}_{k=0}^{K-1}$. Combining Eqs. (66) and (65), random phase rotations can be calibrated for the general case with arbitrary time-frequency hopping patterns.

In Sections F.2 and F.3, we have focused on the coherent combining where multiple subbands are treated as a single larger band for channel and TOA estimation. Analysis indicates that when phase rotations of subbands are calibrated, coherent combining can achieve the resolution facilitated by the entire bandwidth. In comparison, noncoherent combining first estimates the CIR and/or TOA for each subband and then averages subband estimates for a better final estimate. Analysis proves that noncoherent combining can reduce the mistiming probability of TOA estimation when more subbands are used. Noncoherent combining does not require the calibration of random phase rotations and its computational complexity is lower than coherent combining. However, it can only obtain the resolution facilitated by subband bandwidth.

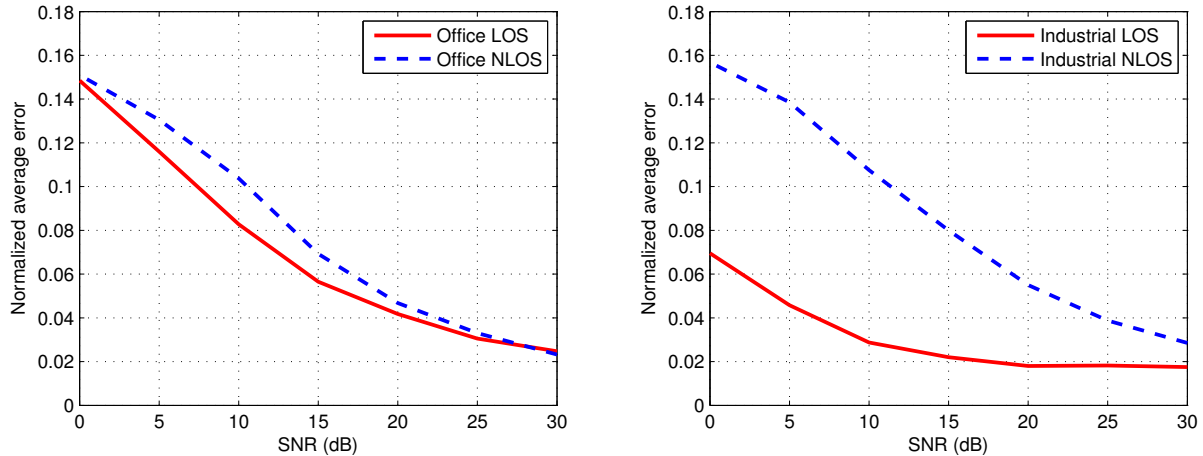


Figure 13: (a) Phase calibration performance for IEEE 802.15.4a office channels.(b) Phase calibration performance for IEEE 802.15.4a industrial channels.

F.4 Simulations

The proposed phase rotation calibration algorithm is simulated based on the ECMA-368 MB-OFDM system in IEEE 802.15.4a UWB channels. Channel information from the first two subbands are coherently combined to estimate the time domain channel. $M = 4$ samples are used to calculate the energy leakage dispersed prior to the first channel path (see (64)).

Figs. 13(a) and 13(b) show performance for the IEEE 802.15.4a office and industrial channels including both the line-of-sight (LOS) and non-line-of-sight (NLOS) scenarios. Phase calibration errors normalized by 2π are plotted versus the signal-to-noise ratio (SNR). For both channel types, performance in the LOS scenario is better than the corresponding NLOS scenario. This is because that in LOS channels, the first channel path is strong and energy leakage (64) is dominated by the first path, which makes LOS channels more like single path channels. Since the energy leakage based algorithm works perfectly for single path channels, the LOS performance should be better than NLOS.

F.5 Summary

In this work, we solved the random phase rotation problem which is encountered in the coherent combining of MB channel information for high resolution TOA estimation. Our analysis indicates that in the presence of random phase rotation, resolution of MB signals degrades due to the increased energy leakage in the channel estimate. Based on this, we

propose to calibrate random phase rotations of subbands by minimizing energy leakage. Simulation results show that our algorithm works well in IEEE 802.15.4a UWB channels.

G From Ranging to Localization: Cooperative Localization via SDP

Recently, GPS-complementary location-aware sensor networks have attracted increasing interests in a wide range of applications such as earthquake detection, weather forecasting, current flow measurement. Such networks typically consist of two types of sensors: the *anchors* or base stations with self-positioning capability, and the *targets* with their positions unknown to the system. The *localization problem* amounts to estimating the locations of the targets based on the known positions of the anchors and geometrical relationships among the sensors.

In conventional wireless systems, such as cellular networks, localization is achieved in a non-cooperative manner; that is, target positions are estimated only by the anchors within the localization range. However, sensor networks can adopt a cooperative mode where inter-target communications are also permitted such that targets can even utilize location information of the anchors outside of the direct communications range and single-hop connections to anchors are no longer a must. While not all targets can estimate their locations non-cooperatively, more of them may cooperatively locate themselves. Cooperative localization not only reduces the density of the expensive anchors but also provides improved localization accuracy. Semidefinite programming (SDP) technique is widely adopted to convert the original nonconvex problems into convex ones in recent years. Time-of-Arrival (ToA) based Standard SDP (SSDP) was proposed in the literature. However, SSDP is not inherently suitable for large-scale networks since the arithmetic operation complexity of SDP is at least $O(k^3)$, where k is the dimension of the semidefinite cones. This also indicates that the semidefinite cones play an important role in further reducing the complexity of SDP. In some other work, Edge-based SDP (ESDP) and Node-based SDP (NSDP) algorithms were proposed as further relaxations of SSDP using ToA measurements. This method of relaxing a set of low-dimensional cones instead of a single high-dimensional cone was computationally desirable. Minimax SDP applicable to both ToA and Received Signal Strength (RSS) models was also proposed.

Fundamental limits of non-cooperative and cooperative localization with ToA measurements were exploited recently. In this research, the Cramér-Rao Lower Bound (CRLB) is tailored for our SDP algorithms in terms of the system models. Besides the CRLB for ToA measurements, we also derive the CRLB for RSS measurements. These CRLBs are further used to show that cooperative localization has the potential to outperform non-cooperative localization. Our minimax Component-wise SDP (CSDP) algorithm is applicable to both ToA and RSS models in both cooperative and non-cooperative setups. Here, we investigate the effects of semidefinite cones in terms of accuracy and efficiency of the cooperative localization algorithms with both ToA and RSS measurements. Effects of SSDP, ESDP, NSDP and CSDP are explored and analyzed to show that our CSDP is the best among them, it is efficient while retaining the crucial theoretical properties of the SDP. Simulations will be performed to verify all our analyses.

G.1 Cooperative Localization Algorithms

In a sensor network localization system with M anchors and N targets in a D dimensional real Euclidean space \mathcal{R}^D ($D = 2$ or 3), locations of the anchors constitute a known vector set $\mathcal{V}_a := \{\mathbf{a}_1, \mathbf{a}_2, \dots, \mathbf{a}_M\}$, and locations of the targets form an unknown vector set $\mathcal{V}_x := \{\mathbf{x}_1, \mathbf{x}_2, \dots, \mathbf{x}_N\}$, with all vectors D -dimensional. Furthermore, we are given the Euclidean distances d_{mn} between \mathbf{a}_m and \mathbf{x}_n for some (m, n) , and \bar{d}_{ij} between \mathbf{x}_i and \mathbf{x}_j for some (i, j) . Specifically, let $\mathcal{E}_a := \{\forall (m, n) : \mathbf{a}_m \in \mathcal{V}_a, \mathbf{x}_n \in \mathcal{V}_x, d_{mn} \text{ is specified}\}$, $\mathcal{E}_x := \{\forall (i, j) : \mathbf{x}_i, \mathbf{x}_j \in \mathcal{V}_x, \bar{d}_{ij} \text{ is specified and } i < j\}$. The *localization problem* in \mathcal{R}^D for the undirected graph $\mathcal{G} := (\mathcal{V}, \mathcal{E})$, where $\mathcal{V} := \mathcal{V}_a \cup \mathcal{V}_x$, $\mathcal{E} := \mathcal{E}_a \cup \mathcal{E}_x$, is to determine the coordinates of the unknown target positions \mathcal{V}_x from the known anchor positions \mathcal{V}_a and the partial distance measurements \mathcal{E} .

Notation: $|\cdot|$ denotes the absolute value, $\|\cdot\|$ denotes the l^2 vector norm, $\text{tr}\{\cdot\}$ is the trace of a square matrix, $(\cdot)^T$ is the matrix transpose operator, and $\text{diag}(\cdot)$ represents a diagonal matrix. Boldface lowercase letters denote vectors, boldface uppercase letters denote matrices. Specifically, $\mathbf{0}$ denotes an all zero entry vector, \mathbf{e}_i denotes an N dimensional vector with all of its entries zero except a unit entry at the i -th position, $\mathbf{I}_{D \times D}$ denotes a $D \times D$ -dimensional identity matrix. Vector and matrix dimensions will be clear in the context, and will be specified whenever necessary. $\mathbf{Z} \succeq 0$ means that \mathbf{Z} is positive semidefinite (PSD), where \mathbf{Z} is a square matrix. $\mathbf{Z}_{(i_1, \dots, i_k)}$ denotes the principal submatrix of \mathbf{Z} from its rows

and columns indexed by i_1, \dots, i_k . $|\mathcal{A}|$ denotes the number of elements in the set \mathcal{A} . $\mathcal{A} \setminus \mathcal{B}$ means the set difference $\{\mathbf{x} | \mathbf{x}_i \in \mathcal{A} \cap \mathbf{x}_i \notin \mathcal{B}\}$.

Distances are measured so long as the node pairs are within the communications range of each other. Suppose there are K available distances, out of which \bar{K} are between one target and one anchor, and the remaining are between two targets.

G.1.1 ToA

Without loss of generality, we can denote the target-anchor distances as

$$d_{mn}^2 = \|\mathbf{a}_m - \mathbf{x}_n\|^2 + \mathfrak{m}_{mn}, \forall (m, n) \in \mathcal{E}_a, \quad (67)$$

and represent the target-target distances as

$$\bar{d}_{ij}^2 = \|\mathbf{x}_i - \mathbf{x}_j\|^2 + \bar{\mathfrak{m}}_{ij}, \forall (i, j) \in \mathcal{E}_x \text{ and } i < j, \quad (68)$$

where noises \mathfrak{m}_{mn} and $\bar{\mathfrak{m}}_{ij}$ are i.i.d. Gaussian distributed with zero mean and variance σ^2 .

Denote the residue vector as $\boldsymbol{\varepsilon} = [\varepsilon_1, \varepsilon_2, \dots, \varepsilon_{\bar{K}}, \varepsilon_{\bar{K}+1}, \varepsilon_{\bar{K}+2}, \dots, \varepsilon_K] = [\varepsilon_{mn}, \dots, \bar{\varepsilon}_{ij}, \dots] = [d_{mn}^2 - \|\mathbf{a}_m - \mathbf{x}_n\|^2, \dots, \bar{d}_{ij}^2 - \|\mathbf{x}_i - \mathbf{x}_j\|^2, \dots]$, and $\mathbf{X}_{D \times N} = [\mathbf{x}_1, \mathbf{x}_2, \dots, \mathbf{x}_N]$, then the conditional probability density function of the measured distances is

$$\begin{aligned} & p(d_{mn}^2, \dots, \bar{d}_{ij}^2, \dots | \mathbf{X}) \\ &= \frac{1}{(2\pi\sigma^2)^{K/2}} e^{-\frac{\sum_{\forall (m,n) \in \mathcal{E}_a} \varepsilon_{mn}^2 + \sum_{\forall (i,j) \in \mathcal{E}_x \text{ and } i < j} \bar{\varepsilon}_{ij}^2}{2\sigma^2}}, \end{aligned} \quad (69)$$

where $\sum_{\forall (m,n) \in \mathcal{E}_a} \varepsilon_{mn}^2$ represents the traditional non-cooperative information, and $\sum_{\forall (i,j) \in \mathcal{E}_x \text{ and } i < j} \bar{\varepsilon}_{ij}^2$ represents the cooperative information.

The Maximum Likelihood (ML) estimate of \mathbf{X} is

$$\hat{\mathbf{X}} = \arg \min_{\mathbf{X}} \sum_{\forall (m,n) \in \mathcal{N}_a} \varepsilon_{mn}^2 + \sum_{\forall (i,j) \in \mathcal{N}_x \text{ and } i < j} \bar{\varepsilon}_{ij}^2 = \arg \min_{\mathbf{X}} \|\boldsymbol{\varepsilon}\|^2. \quad (70)$$

Note that $\hat{\mathbf{X}}$ is optimal in the ML sense.

The optimization problem of (70) is highly nonlinear and nonconvex in \mathbf{X} , thus difficult to solve. In this work, we use minimax relaxation and semidefinite relaxation to convert the original nonconvex problems into convex ones. Denote $\mathbf{Y} = \mathbf{X}^T \mathbf{X}$, and approximate this nonlinear and nonconvex equation via semidefinite relaxation $\mathbf{Y} \succeq \mathbf{X}^T \mathbf{X}$. The result is still nonlinear but already convex. The minimax SDP algorithm for ToA measurements² is

$$\min_{t, \mathbf{Z}} t \quad (71)$$

²Suppose all targets are localizable. Localizability itself is a challenging research area which is beyond the scope of this work.

$$\begin{aligned}
& \text{s.t. } -t < \text{tr} \left\{ \begin{pmatrix} -\mathbf{a}_m \\ \mathbf{e}_n \end{pmatrix} \begin{pmatrix} -\mathbf{a}_m^T & \mathbf{e}_n^T \end{pmatrix} \cdot \mathbf{Z} \right\} - d_{mn}^2 < t, \\
& -t < \text{tr} \left\{ \begin{pmatrix} \mathbf{0}_{D \times 1} \\ \mathbf{e}_i - \mathbf{e}_j \end{pmatrix} \begin{pmatrix} \mathbf{0}_{1 \times D} & (\mathbf{e}_i - \mathbf{e}_j)^T \end{pmatrix} \cdot \mathbf{Z} \right\} - \bar{d}_{ij}^2 < t, \\
& \quad \forall (m, n) \in \mathcal{E}_a, \forall (i, j) \in \mathcal{E}_x \text{ and } i < j, \\
& \mathbf{Z}_{(1:D)} = \mathbf{I}_{D \times D}, \mathbf{Z}_{(1:D,i)} \succeq 0, \forall \mathbf{x}_i \in \mathcal{V}_x \setminus \mathcal{X}, \\
& \mathbf{Z}_{(1:D,i,j)} \succeq 0, \forall (i, j) \in \mathcal{E}_x \text{ and } i < j.
\end{aligned}$$

G.1.2 RSS

In the ideal case, each target node emits a signal with power P , and anchor nodes within the localization range can receive a signal with energy strength

$$s_{mn} = P \|\mathbf{a}_m - \mathbf{x}_n\|^{-\beta}, \forall (m, n) \in \mathcal{E}_a, \quad (72)$$

and target nodes within the localization range can receive a signal with energy strength

$$\bar{s}_{ij} = P \|\mathbf{x}_i - \mathbf{x}_j\|^{-\beta}, \forall (i, j) \in \mathcal{E}_x \text{ and } i < j, \quad (73)$$

where β is the path loss coefficient.

Under the lognormal fading channel, the RSS in dB can be modeled as

$$10 \log s_{mn} = 10 \log P - 10\beta \log(\|\mathbf{a}_m - \mathbf{x}_n\|) + \mathfrak{m}_{mn}, \quad (74)$$

$\forall (m, n) \in \mathcal{E}_a$ for target-anchor connections and

$$10 \log \bar{s}_{ij} = 10 \log P - 10\beta \log(\|\mathbf{x}_i - \mathbf{x}_j\|) + \bar{\mathfrak{m}}_{ij}, \quad (75)$$

$\forall (i, j) \in \mathcal{E}_x$ and $i < j$ for target-target connections, where \mathfrak{m}_{mn} and $\bar{\mathfrak{m}}_{ij}$ are assumed to be i.i.d. Gaussian distributed noises with zero mean and variance σ^2 .

Denote the residue vector as $\boldsymbol{\epsilon} = [\epsilon_1, \epsilon_2, \dots, \epsilon_{\bar{K}}, \epsilon_{\bar{K}+1}, \epsilon_{\bar{K}+2}, \dots, \epsilon_K] = [\epsilon_{mn}, \dots, \bar{\epsilon}_{ij}, \dots] = [\ln s_{mn} - \ln(\frac{P}{\|\mathbf{a}_m - \mathbf{x}_n\|^\beta}), \dots, \ln \bar{s}_{ij} - \ln(\frac{P}{\|\mathbf{x}_i - \mathbf{x}_j\|^\beta}), \dots]$, the conditional probability density function of the RSS in dB is

$$\begin{aligned}
& p(\ln s_{mn}, \dots, \ln \bar{s}_{ij}, \dots | \mathbf{X}) \\
& = \frac{1}{(2\pi(\frac{\sigma \ln 10}{10})^2)^{K/2}} e^{-\frac{\sum_{\forall (m,n) \in \mathcal{E}_a} \epsilon_{mn}^2 + \sum_{\forall (i,j) \in \mathcal{E}_x} \bar{\epsilon}_{ij}^2}{2(\frac{\sigma \ln 10}{10})^2}}, \quad (76)
\end{aligned}$$

where $\sum_{\forall (m,n) \in \mathcal{E}_a} \epsilon_{mn}^2$ represents the traditional non-cooperative information, and $\sum_{\forall (i,j) \in \mathcal{E}_x \text{ and } i < j} \bar{\epsilon}_{ij}^2$ represents the cooperative information.

The ML estimate of \mathbf{X} can be obtained as

$$\hat{\mathbf{X}} = \arg \min_{\mathbf{X}} \sum_{\forall (m,n) \in \mathcal{N}_a} \epsilon_{mn}^2 + \sum_{\forall (i,j) \in \mathcal{N}_x} \bar{\epsilon}_{ij}^2 = \arg \min_{\mathbf{X}} \|\epsilon\|^2. \quad (77)$$

Note that $\hat{\mathbf{X}}$ is optimal in the ML sense.

Again, the optimization problem of (77) is highly nonlinear and nonconvex in \mathbf{X} , thus difficult to solve. Similar to the ToA case, we adopt an minimax SDP approach to convert the original nonconvex problems into convex ones. The minimax SDP algorithm for RSS measurements is

$$\begin{aligned} & \min_{t, \mathbf{Z}} t & (78) \\ \text{s.t. } & -t < q_{mn} \cdot \text{tr} \left\{ \begin{pmatrix} -\mathbf{a}_m \\ \mathbf{e}_n \end{pmatrix} \begin{pmatrix} -\mathbf{a}_m^T & \mathbf{e}_n^T \end{pmatrix} \cdot \mathbf{Z} \right\} - 1 < t, \\ & -t < \bar{q}_{ij} \cdot \text{tr} \left\{ \begin{pmatrix} \mathbf{0}_{D \times 1} \\ \mathbf{e}_i - \mathbf{e}_j \end{pmatrix} \begin{pmatrix} \mathbf{0}_{1 \times D} & (\mathbf{e}_i - \mathbf{e}_j)^T \end{pmatrix} \cdot \mathbf{Z} \right\} - 1 < t, \\ & \forall (m, n) \in \mathcal{E}_a, \forall (i, j) \in \mathcal{E}_x \text{ and } i < j, \\ & \mathbf{Z}_{(1:D)} = \mathbf{I}_{D \times D}, \mathbf{Z}_{(1:D,i)} \succeq 0, \forall \mathbf{x}_i \in \mathcal{V}_x \setminus \mathcal{X}, \\ & \mathbf{Z}_{(1:D,i,j)} \succeq 0, \forall (i, j) \in \mathcal{E}_x \text{ and } i < j. \end{aligned}$$

In (71) and (78) $\mathcal{X} = \{\mathbf{x}_i | \forall i, \exists (i, j) \in \mathcal{E}_x, i < j \cup (n, i) \in \mathcal{E}_x, n < i\}$ is the set formed by all the targets that have other target(s) as neighbor(s). The first conic constraint for those $\mathbf{x}_i \in \mathcal{X}$ is redundant, since it is implied by the second conic constraint. Once the solutions of (71) and (78) are found, the upper right $D \times N$ corners of \mathbf{Z} are taken out as the semidefinite approximated location estimate $\tilde{\mathbf{X}}$.

G.2 Cramér-Rao Lower Bound

Here, we derive the Cramér-Rao Lower Bound (CRLB) for both cooperative and non-cooperative scenarios with both ToA and RSS measurements according to our system models. These CRLBs are then used to make comparisons between cooperative localization and non-cooperative localization.

G.2.1 ToA

Let $\mathbb{z}_{ToA} = [d_{mn}^2, \dots, \bar{d}_{ij}^2, \dots]^T$ be a vector that contains all measurements. From (69), we see that \mathbb{z}_{ToA} is Gaussian distributed with mean $\boldsymbol{\mu}_{ToA}$ and covariance matrix \mathbf{C}_{ToA}

$$\begin{aligned}\boldsymbol{\mu}_{ToA} &= [\|\mathbf{a}_m - \mathbf{x}_n\|^2, \dots, \|\mathbf{x}_i - \mathbf{x}_j\|^2, \dots]^T, \\ \mathbf{C}_{ToA} &= \text{diag}(\sigma^2, \dots, \sigma^2, \dots).\end{aligned}\quad (79)$$

The Fisher information matrix (FIM) has elements

$$\begin{aligned}\mathbf{I}_{i,j}^{ToA} &= \frac{\partial \boldsymbol{\mu}_{ToA}^T}{\partial \mathbf{x}_i} \mathbf{C}_{ToA}^{-1} \frac{\partial \boldsymbol{\mu}_{ToA}}{\partial \mathbf{x}_j} \\ &\quad + \frac{1}{2} \text{tr} \left\{ \mathbf{C}_{ToA}^{-1} \frac{\partial \mathbf{C}_{ToA}}{\partial \mathbf{x}_i} \mathbf{C}_{ToA}^{-1} \frac{\partial \mathbf{C}_{ToA}}{\partial \mathbf{x}_j} \right\}, \\ &\quad i, j = 1, 2, \dots, N.\end{aligned}\quad (80)$$

Considering given assumptions in our ToA model, the FIM is

$$\mathbf{I}^{ToA} = 4\sigma^{-2} \mathbb{I}^{ToA}. \quad (81)$$

Diagonal terms of \mathbb{I}^{ToA} are

$$\begin{aligned}\mathbb{I}_{nn}^{ToA} &= \sum_{m, \forall (m,n) \in \mathcal{E}_a} d_{mn}^2 + \sum_{i, \forall (i,n) \in \mathcal{E}_x \text{ and } i < n} \bar{d}_{in}^2 \\ &\quad + \sum_{j, \forall (n,j) \in \mathcal{E}_x \text{ and } n < j} \bar{d}_{nj}^2, \quad n = 1, 2, \dots, N,\end{aligned}\quad (82)$$

and off-diagonal terms are

$$\mathbb{I}_{ij}^{ToA} = \mathbb{I}_{ji}^{ToA} = -\bar{d}_{ij}^2, \quad \forall (i,j) \in \mathcal{E}_x \text{ and } i < j. \quad (83)$$

Diagonal terms are contributed by all connections, including both the cooperative and the non-cooperative connections, while off-diagonal terms display the effects of the cooperative links. Thus elements of \mathbb{I}^{ToA} for the non-cooperative case with ToA measurements only contains non-zero diagonal terms

$$\mathbb{I}_{nn}^{ToA} = \sum_{m, \forall (m,n) \in \mathcal{E}_a} d_{mn}^2, \quad n = 1, 2, \dots, N, \quad (84)$$

with all off-diagonal terms zero.

Suppose every targets is connected to at least one anchor, then \mathbb{I}^{ToA} is a strictly diagonally dominant matrix. By Levy-Desplanques theorem, \mathbb{I}^{ToA} is non-singular.³ Thus, the CRLB for \mathbf{X} with ToA measurements can be obtained from the diagonal elements of the inverse matrix of \mathbf{I}^{ToA} .

³If a target has no target-anchor connections, then without cooperative information, it will be an isolated non-localizable node. Here we do not consider this type of cooperative vs. non-cooperative comparisons.

G.2.2 RSS

Denote $\mathbb{z}_{RSS} = [\ln s_{mn}, \dots, \ln \bar{s}_{ij}, \dots]^T$. From (76), \mathbb{z}_{RSS} is Gaussian distributed with mean $\boldsymbol{\mu}_{RSS} = [\ln(\frac{P}{\|\mathbf{a}_m - \mathbf{x}_n\|^\beta}), \dots, \ln(\frac{P}{\|\mathbf{x}_i - \mathbf{x}_j\|^\beta}), \dots]^T$ and covariance matrix $\mathbf{C}_{RSS} = \text{diag}((\frac{\sigma \ln 10}{10})^2, \dots, (\frac{\sigma \ln 10}{10})^2, \dots)$. Similarly, the FIM is

$$\mathbf{I}^{RSS} = (\frac{10\beta}{\ln 10})^2 \sigma^{-2} \mathbb{I}^{RSS}. \quad (85)$$

Where

$$\begin{aligned} \mathbb{I}_{nn}^{RSS} &= \sum_{m, \forall (m,n) \in \mathcal{E}_a} \frac{1}{d_{mn}^2} + \sum_{i, \forall (i,n) \in \mathcal{E}_x \text{ and } i < n} \frac{1}{d_{in}^2} \\ &+ \sum_{j, \forall (n,j) \in \mathcal{E}_x \text{ and } n < j} \frac{1}{d_{nj}^2}, n = 1, 2, \dots, N, \end{aligned} \quad (86)$$

and

$$\mathbb{I}_{ij}^{RSS} = \mathbb{I}_{ji}^{RSS} = -\frac{1}{d_{ij}^2}, \forall (i, j) \in \mathcal{E}_x \text{ and } i < j. \quad (87)$$

Similarly, elements of \mathbb{I}^{RSS} for the non-cooperative case with RSS measurements only involves non-zero diagonal terms

$$\mathbb{I}_{nn}^{RSS} = \sum_{m, \forall (m,n) \in \mathcal{E}_a} \frac{1}{d_{mn}^2}, n = 1, 2, \dots, N, \quad (88)$$

with all off-diagonal terms zero.

We can then get the CRLB for \mathbf{X} with RSS measurements from the inverse matrix of the FIM \mathbf{I}^{RSS} .

G.2.3 Cooperative vs. Non-cooperative Localization

Based on the CRLB derived in Section G.2.1 and G.2.2, we show that performance bounds of cooperative algorithms will never be above the non-cooperative counterparts.

Theorem 1 *The Cramér-Rao Lower Bound (CRLB) of the cooperative localization is lower than or equal to that of the non-cooperative localization.*

$$\begin{aligned} \text{CRLB}_{\text{Coop}}^{\text{ToA}} &\leq \text{CRLB}_{\text{Noncoop}}^{\text{ToA}} \\ \text{CRLB}_{\text{Coop}}^{\text{RSS}} &\leq \text{CRLB}_{\text{Noncoop}}^{\text{RSS}}. \end{aligned} \quad (89)$$

Proof: Denote eigenvalues of \mathbb{I}^{ToA} as $\lambda_1, \lambda_2, \dots, \lambda_N$. By Geršgorin disc theorem ,

$$|\lambda_n - \mathbb{I}_{nn}^{\text{ToA}}| \leq \sum_{i \neq n} |\mathbb{I}_{ni}^{\text{ToA}}|, n = 1, 2, \dots, N. \quad (90)$$

For those x_n 's that have no cooperative connections

$$\lambda_n = \sum_{m, \forall (m,n) \in \mathcal{E}_a} d_{mn}^2, \quad (91)$$

and for those x_n 's that have cooperative connections

$$\lambda_n > \sum_{m, \forall (m,n) \in \mathcal{E}_a} d_{mn}^2. \quad (92)$$

Hence, eigenvalues of the inverse matrix of \mathbb{I}^{ToA} are

$$\lambda_n^{-1} = \frac{1}{\sum_{m, \forall (m,n) \in \mathcal{E}_a} d_{mn}^2} \quad (93)$$

for those x_n 's that have no cooperative connections and

$$\lambda_n^{-1} < \frac{1}{\sum_{m, \forall (m,n) \in \mathcal{E}_a} d_{mn}^2} \quad (94)$$

for those x_n 's that have cooperative connections.

From (93) and (94), we conclude that

$$\text{CRLB}_{\text{Coop}}^{\text{ToA}} \leq \text{CRLB}_{\text{Noncoop}}^{\text{ToA}}. \quad (95)$$

Similarly, for RSS measurements

$$\text{CRLB}_{\text{Coop}}^{\text{RSS}} \leq \text{CRLB}_{\text{Noncoop}}^{\text{RSS}}. \quad (96)$$

For both ToA and RSS measurements, we get the conclusion that cooperative algorithms have the potential to outperform non-cooperative ones.

G.3 Effects of Semidefinite Cones

Since objective functions and all inequality constraints of various minimax SDP algorithms remain the same, to compare minimax SDP algorithms, we only need to compare all the existing and our proposed semidefinite cones. We then investigate into effects of semidefinite cones on efficiency and accuracy of the cooperative localization algorithms.

G.3.1 Types of Semidefinite Cones

Standard Semidefinite Cones

Standard semidefinite approximation is $\mathbf{Y} = \mathbf{X}^T \mathbf{X} \Rightarrow \mathbf{Y} \succeq \mathbf{X}^T \mathbf{X}$, i.e., the standard semidefinite cone is

$$\mathbf{Z} = \begin{pmatrix} \mathbf{I}_{D \times D} & \mathbf{X}_{D \times N} \\ \mathbf{X}_{N \times D}^T & \mathbf{Y}_{N \times N} \end{pmatrix} \succeq 0. \quad (97)$$

Further Relaxations to Standard Semidefinite Cones

- Edge-based Semidefinite Cones

$$\mathbf{Z}_{(1:D,i,j)} \succeq 0, \forall (i,j) \in \mathcal{E}_x. \quad (98)$$

- Node-based Semidefinite Cones

$$\mathbf{Z}_{(1:D,i,\mathcal{N}_{\mathbf{x}_i})} \succeq 0, \forall \mathbf{x}_i \in \mathcal{V}_x. \quad (99)$$

where $\mathcal{N}_{\mathbf{x}_i} = \{j : (i,j) \in \mathcal{E}_x, i < j \text{ or } (j,i) \in \mathcal{E}_x, j < i\}$ is the set formed by all the targets connected to \mathbf{x}_i .

- Component-wise Semidefinite Cones (our proposed)

$$\begin{aligned} \mathbf{Z}_{(1:D,i)} &\succeq 0, \forall \mathbf{x}_i \in \mathcal{V}_x \setminus \mathcal{X}. \\ \mathbf{Z}_{(1:D,i,j)} &\succeq 0, \forall (i,j) \in \mathcal{E}_x. \end{aligned} \quad (100)$$

G.3.2 Performance comparisons

In the literature, it has been shown that $F^{SSDP} \subset F^{NSDP} \subset F^{ESDP}$, where F represents the solution set of the corresponding SDP algorithm. For our proposed CSDP, we have the following result.

Proposition 7 *The solution sets of NSDP, CSDP and ESDP follow the following relationship:*

$$F^{NSDP} \subset F^{CSDP} \subset F^{ESDP}. \quad (101)$$

Proof Denote solutions to (99), (100) and (98) as \mathbf{Z}_{NSDP}^* , \mathbf{Z}_{CSDP}^* and \mathbf{Z}_{ESDP}^* , respectively. NSDP contains redundancy because it assumes that all pairwise connections of $\mathcal{N}_{\mathbf{x}_i}$ exist, which is not necessarily true. After removing these unspecified variables in \mathbf{Z}_{NSDP}^* , one would obtain \mathbf{Z}_{CSDP}^* . Similarly, after removing the non-cooperative constraints in \mathbf{Z}_{CSDP}^* , one would obtain \mathbf{Z}_{ESDP}^* .

To further explore the performances of these SDP algorithms, let us first introduce some definitions.

Definition 1 An undirected graph is a chordal graph if every cycle of length greater than three has a chord. An equivalent definition is that any chordless cycles have at most three nodes.

Definition 2 A square matrix, possibly containing some unspecified entries, is called partial symmetric if whenever the (i, j) -th entry of the matrix is specified, then so is the (j, i) -th entry, and the two are equal. A partial semidefinite matrix is a partial symmetric matrix for which every fully specified principal submatrix is positive semidefinite.

Given these, we can now introduce the following Lemma.

Lemma 2 Every partial positive semidefinite matrix with undirected graph $\bar{\mathcal{G}}$ has positive semidefinite completion if and only if $\bar{\mathcal{G}}$ is chordal.

Based on the above proposition, definitions and lemma, we have the following theorem.

Theorem 2 If the undirected graph $\mathcal{G}_x := (\mathcal{V}_x, \mathcal{E}_x)$ induced by all the targets is chordal, then

$$F^{SSDP} = F^{CSDP}. \quad (102)$$

Proof: By Proposition 7, we only need to prove that any solution to (100) can be completed to a solution of (97). Suppose

$$\mathbf{Z} = \begin{pmatrix} \mathbf{I} & \mathbf{X} \\ \mathbf{X}^T & \mathbf{Y} \end{pmatrix} \quad (103)$$

is a solution of (100). By Definition 2, \mathbf{Z} is a partial semidefinite matrix.

By the prerequisite, the undirected graph induced by \mathbf{Y} is chordal. We now prove that the undirected graph induced by \mathbf{Z} is also chordal. Notice that the graph induced by \mathbf{Z} has $N + D$ nodes, with every specified off-diagonal entry denoting an edge. Every one of the first D nodes in the graph induced by \mathbf{Z} is connected to every target node in \mathcal{V}_x . If a cycle in the graph induced by \mathbf{Z} contains some or all of the first D nodes, then it must have a chord since each of the first D nodes is connected to every target; if the cycle does not contain any of the first D nodes, then it must still contain a chord because the graph induced by \mathbf{Y} is chordal. Thus, the graph induced by \mathbf{Z} is chordal. By Lemma 2, \mathbf{Z} must have a positive semidefinite completion $\bar{\mathbf{Z}}$. Considering that (97) and (100) share the same constraints specified by the existing connections, $\bar{\mathbf{Z}}$ must be a solution to (97).

For chordal graphs \mathcal{G}_x , we do not lose any relevant information in CSDP, thus SSDP and CSDP are equivalent. Notice that we only need \mathcal{G}_x to be chordal, not requiring that the

whole localization graph \mathcal{G} to be chordal. Furthermore, by Proposition 7 and Theorem 2, one can easily deduce that

$$F^{SSDP} = F^{NSDP} \quad (104)$$

for a chordal graph \mathcal{G}_x , which coincides with the results in the existing literature.

These result essentially confirm that, containing reduced constraints, CSDP leads to identical solutions as SSDP and NSDP. In other words, both SSDP and NSDP contain redundant variables, and these redundant elements increase the complexity, thus have negative impacts on the localization efficiency. ESDP is theoretically deficient, because the removed $D + 1$ -dimensional conic constraints in (98) in the proof of Proposition 7 are necessary information. ESDP only retains cooperative information while loses non-cooperative information.

G.3.3 Complexity comparisons

In Table 1, we list the computational complexity of various SDP localization algorithms. Note that, $\sum_{i=1}^N (D + 1 + |\mathcal{N}_{\mathbf{x}_i}|)^2$, $|\mathcal{E}_x|(D + 2)^2$, and $(N - |\mathcal{X}|)(D + 1)^2 + |\mathcal{E}_x|(D + 2)^2$ are typically much smaller than $(N + D)^2$. Hence, with a much smaller number of variables, NSDP, ESDP and CSDP have the potential to reduce the computational complexity compared to SSDP, especially for large N .

Table 1: SDP localization algorithm complexity analysis

	Number of Conic Constraints	Dimension of Cones	Number of Variables	Number of Equality Constraints
SSDP	1	$N + D$	$(N + D)^2$	$ \mathcal{E}_a + \mathcal{E}_x $
NSDP	N	$D + 1 + \mathcal{N}_{\mathbf{x}_i} $	$\sum_{i=1}^N (D + 1 + \mathcal{N}_{\mathbf{x}_i})^2$	$ \mathcal{E}_a + \mathcal{E}_x $
ESDP	$ \mathcal{E}_x $	$D + 2$	$ \mathcal{E}_x (D + 2)^2$	$ \mathcal{E}_a + \mathcal{E}_x $
CSDP	$N - \mathcal{X} + \mathcal{E}_x $	$D + 1, D + 2$	$(N - \mathcal{X})(D + 1)^2 + \mathcal{E}_x (D + 2)^2$	$ \mathcal{E}_a + \mathcal{E}_x $

Generally speaking, ESDP, NSDP and CSDP are all further relaxations of SSDP. Even though SSDP is more accurate and may possess a better efficacy for small-scale networks, it is not suitable for large scale networks since it involves a single high-dimensional semidefinite cone. ESDP loses some useful information, thus it is not robust enough and blows

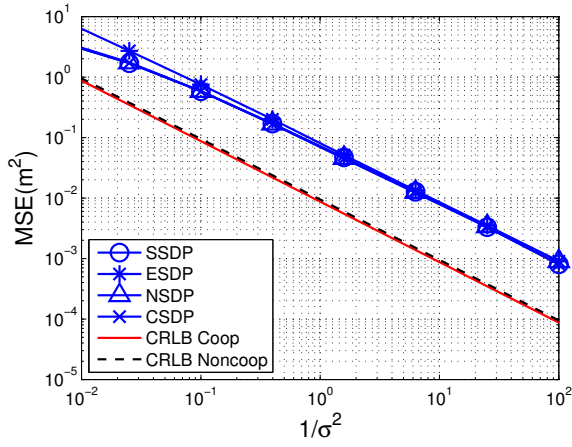
up under severe noisy cases. Even though NSDP involves multiple low-dimensional conic constraints, it contains redundancy. CSDP naturally results from the component-wise formulation of the original problem, keeps all the specified and necessary variables, and only those variables. Thus CSDP can achieve comparable accuracy with reasonable complexity. Moreover, given the complexity analysis, CSDP is suitable for large-scale wireless sensor networks.

G.4 Simulations

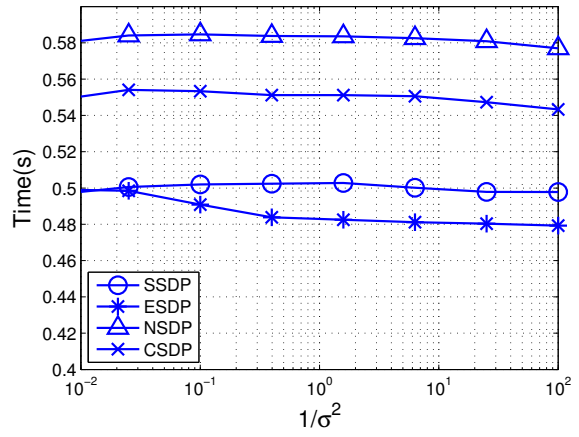
In this section, we use the CVX package as our SDP solvers. Localization accuracy is evaluated by the mean square error ($\text{MSE} = \frac{1}{N} \sum_{n=1}^N \|\tilde{\mathbf{x}}_n - \mathbf{x}_n\|^2$) of the location estimates, and localization efficiency is indicated by the average time used for locating all the targets in the sensor networks. System parameters for RSS measurements are $P = 1000$, $\beta = 3$. All simulation results are averaged over 2000 Monte Carlo tests.

On a 2-D map, anchors are located at $\mathcal{V}_a = \{[0, 6]^T, [0, 0]^T, [2, 4]^T, [6, 0]^T, [7, 7]^T, [8, 0]^T\}$, targets are placed at $\mathcal{V}_x = \{[0, 4]^T, [3, 8]^T, [2, 2]^T, [6, 5]^T, [7, 3]^T\}$. Communications are allowed between node pairs at $\mathcal{E}_a = \{(1, 1), (2, 1), (1, 2), (3, 1), (2, 3), (3, 2), (3, 3), (5, 2), (3, 4), (4, 3), (5, 4), (4, 5), (6, 5)\}$ and $\mathcal{E}_x = \{(4, 5)\}$. Cases, including inside the convex hull, on the edge of the convex hull, out of the convex hull, as well as the cooperation between two targets, are all considered in this localization system. We use the cooperative algorithms to make comparisons, and give the CRLBs for both cooperative and non-cooperative localization showing that the cooperative localization has the potential to outperform the non-cooperative counterpart.

See Figure 14(a) for algorithm accuracy performances and Figure 14(b) for algorithm efficiency performances with ToA measurements. See Figure 15(a) for algorithm accuracy performances and Figure 15(b) for algorithm efficiency performances with RSS measurements. CRLBs are also given as benchmarks, showing that accuracy performances of our SDP algorithms are satisfactory. Our simulation results show that CSDP achieves comparable accuracy with reasonable complexity. Moreover, by adopting cooperative localization, we successfully locate all the targets, including \mathbf{x}_4 and \mathbf{x}_5 , which are not localizable without cooperative information.

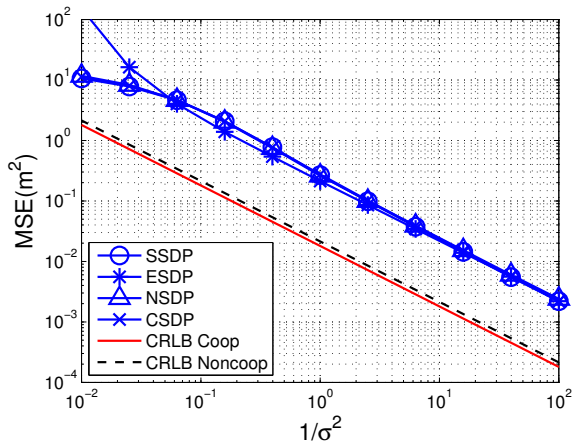


(a)

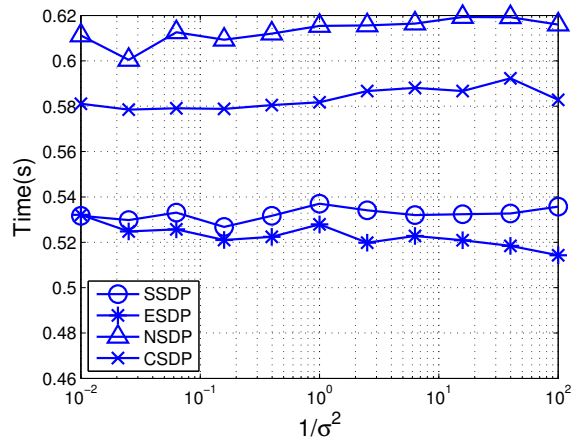


(b)

Figure 14: (a) ToA localization accuracy. (b) ToA localization efficiency.



(a)



(b)

Figure 15: (a) RSS localization accuracy. (b) RSS localization efficiency.

G.5 Summary

In this research, Time-of-Arrival (ToA) and Received Signal Strength (RSS) based minimax semidefinite programming (SDP) algorithms were adopted for cooperative localization where inter-target communication capability was exploited for coverage extension and accuracy enhancement. We derived the Cramér-Rao Lower Bound (CRLB) to verify the benefits of cooperative localization. Various semidefinite algorithms, including Standard SDP (SSDP), Edge-based SDP (ESDP), Node-based SDP (NSDP) and Component-wise SDP (CSDP), were then investigated to show that CSDP was the best among them in terms of localization complexity and accuracy. These theoretical analyses had all been corroborated with simulations.

H From Ranging to Localization: Exploiting Doppler Effects

Traditionally, position of a target can be estimated by measuring one or more of the following quantities: angle-of-arrival (AoA), received signal strength (RSS), and time-of-arrival (ToA). For AoA-based techniques, tracking of the moving target relies on the measurement of the angle of the incoming signal arrival at each anchor node (AN) with antenna array. The AoA is not very suitable for the opportunistic positioning, because the antenna array is usually large and expensive. RSS-based positioning techniques require the knowledge of channel path-loss parameters and are therefore very sensitive to the estimation of these parameters. Compared to AoA and RSS, ToA measurement combined with the triangulation is a more feasible means for wireless positioning in multipath channel environments, especially when broadband signals are used to achieve the high timing resolution. To avoid the need of the common time base between the target and each anchor node, the time difference of arrival (TDoA) technique can be adopted. However, the time base still needs to be calibrated among all anchor nodes.

In order to avoid these problems associated with the traditional methods, we propose a new localization and navigation approach based on the Doppler frequency of the line-of-sight (LoS) path between the moving target (MT) and each AN. As long as the AN is able to identify the LoS component of the multipath channel, it can estimate the Doppler frequency caused by the movement of the target. After the Doppler frequency is measured at each anchor node, the radial velocity which is defined as the relative velocity between

the moving target and each anchor node can be estimated. Suppose that we have N ANs with their location coordinates known to the system. We can establish N equations with the radial velocities and four unknown parameters: the moving direction of the target, the absolute velocity of the target, and the location coordinates of the moving target. Among them, the angle of moving direction and the absolute velocity are two nuisance parameters. Solving these equations, we can obtain the location of the moving target.

Compared to existing techniques, the hardware cost of this positioning method is lower, because no antenna array is needed. In addition, no common time base is assumed either between the moving target and each anchor node or among the anchor nodes. This is a great advantage in comparison with the conventional ToA and TDoA techniques. Besides, our technique benefits from the motion of target, performance improves as velocity increases.

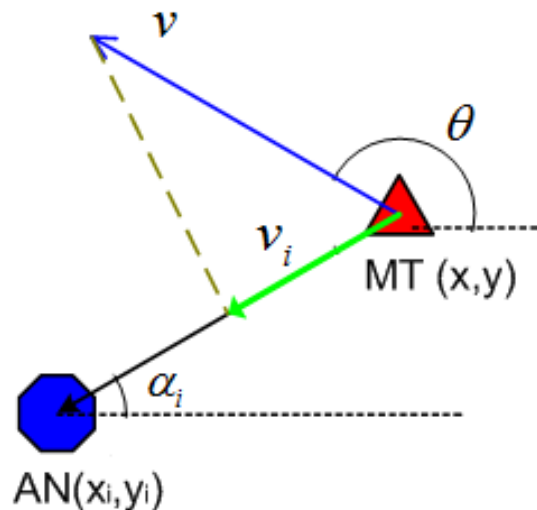


Figure 16: System setup.

H.1 System Description

Suppose we have N anchor nodes (AN) with the location coordinates $\{(x_i, y_i)\}_{i=1}^N$ of the i th AN known a priori to the system. The signal transmission can be either from MT to AN or AN to MT. Our technique can be applied independent of the direction of signal flow. The target moves in a direction θ with a velocity v m/sec. Let α_i be the angle of arrival (AoA) of the signal received at the i th AN, as shown in Fig.16.

Then the radial velocity of the moving target with respect to the i th anchor node is

$$v_i = v \cos(\pi + \alpha_i - \theta) = -v \cos(\alpha_i - \theta) \quad (105)$$

where $i \in [1, N]$, $\alpha_i \in [0, 2\pi)$, and $\theta \in [0, 2\pi)$. Our objective is to recover the location coordinates (x_t, y_t) of the moving target from \hat{v}_i and $\{(x_i, y_i)\}_{i=1}^N$. Solving the nonlinear equation (105) by using measurements of $\{v_i\}_{i=1}^N$, we can estimate the location of the moving target. To show the feasibility of this approach, we first present a very direct approach.

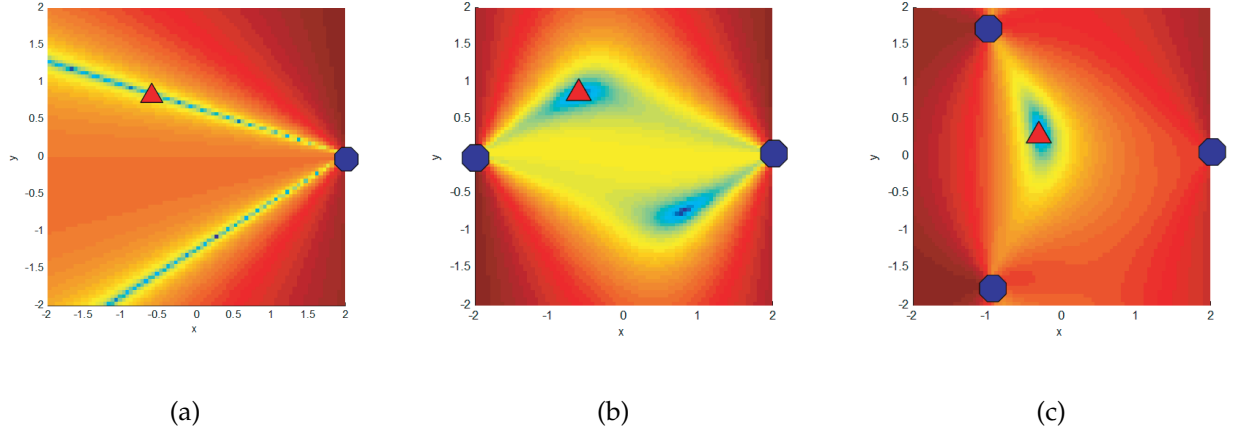


Figure 17: Error of mislocalization (a) 1 anchor node; (b) 2 anchor nodes; (c) 3 anchor nodes.

H.1.1 Straightforward Approach

In the region of interest where MT could possibly reside, we consider every possible candidate location (x', y') . For each candidate location, calculate the radial velocities $\{v'_i\}_{i=1}^N$ at all ANs assuming velocity v and direction θ are known. After calculating the radial velocities for all possible locations, we choose that particular location which gives radial velocities that match closest to the actual radial velocities $\{v_i\}_{i=1}^N$ obtained from the doppler spectrum. For doing this we define the error of mislocalization given by

$$E = \sum_{i=1}^N (v_i - v'_i)^2$$

We plot the error of mislocalization as shown in Fig. 17 for $N = (1, 2, 3)$ anchor nodes that are uniformly located on the circle with the radius of 2, and the target is marked by the red solid triangle. When one anchor node is used, the target can be on either of two half lines where the error is 0. This shows the approach is essentially equivalent to the AoA based technique without any antenna array, the difference being that here we have two half lines. When there are two anchor nodes, the target can be found at the intersection of the ambiguity ranges of the two anchor nodes. Fig. 17 (b) shows that the error surface has two minima in the area of interest. Only one corresponds to the position of the target. The other one is false. As shown in Fig. 17 (c), when three anchor nodes are used, the false solution can be eliminated. This way, the unique location of the moving target can be estimated by determining the minimum peak of the error plot. It should be noted that $\{v_i\}_{i=1}^N$ and (x_t, y_t) vary as the target moves. However, when the anchor nodes are far from the target,

these parameters can be assumed to be constant during one localization processing interval. Though it is pretty straightforward, it is impractical as it is computationally intensive to calculate the mislocalization error for every single candidate location point in such a large area covered by ANs. Thus we should explore for more sophisticated methods for practicality.

Our goal in this work is to estimate the MT location coordinates (x_t, y_t) by solving Eq. (105). As for the solution of this nonlinear equation, no linearization technique has been found. Since among all the unknown parameters, the absolute velocity v and the moving direction θ are two nuisance parameters, if at least one or both of v and θ are known by the ANs, the problem will be significantly simplified. Hence in the following sections we present the solutions to the localization equations with different levels of prior knowledge of v and θ .

H.2 Case I: Known v , Known θ

Consider the case when both the velocity and moving direction of the target are known at the ANs. This scenario could occur when the target is mounted on a vehicle that is moving with a constant speed in the same direction along a straight road. The velocity of the target, v can be read electronically from the speedometer of the vehicle and the moving direction of the target, θ can be obtained from the gyroscope on the vehicle.

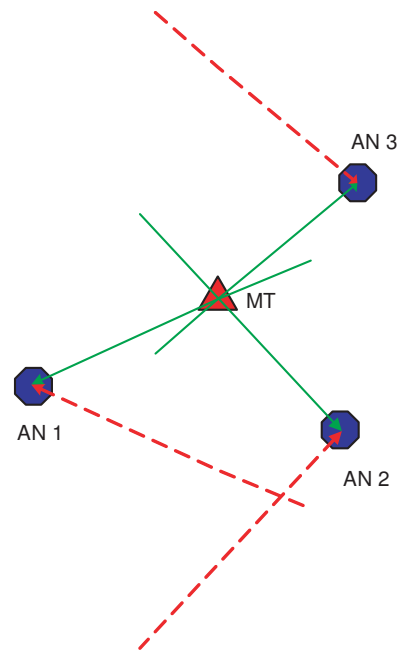


Figure 18: Only the set of correct AoA intersect at the MT location

H.2.1 The Basic Algorithm

Recollect from Eq. (105), when both v and θ are known, we have

$$\cos(\alpha_i - \theta) = -\frac{v_i}{v}, \quad i \in [1, N]. \quad (106)$$

We know $\alpha_i \in [0, 2\pi)$ and $\theta \in [0, 2\pi)$, and hence $(\alpha_i - \theta) \in [-2\pi, 2\pi)$. Let $\gamma_i = \cos^{-1}(-v_i/v)$ be the principal solution. Then $(\alpha_i - \theta)$ is one of the four possible solutions $\{\gamma_i, 2\pi - \gamma_i, -\gamma_i, \gamma_i -$

$2\pi\}$ and hence α_i is one of the four possible solutions $\{\gamma_i + \theta, 2\pi - \gamma_i + \theta, -\gamma_i + \theta, \theta - 2\pi + \gamma_i\}$.

Using the known condition $\alpha_i \in [0, 2\pi)$, we can directly eliminate two among four possible solutions. Now, we are left with two possible solutions of the AoA α_i . Hence, the problem reduces to AoA based location estimation. Only one of the two solutions is the correct AoA. The correct AoA of all the N ANs intersect at a single point which is the actual location of the target. The other angles will never intersect at a single point in ideal scenarios where the noise is absent (see Fig. 18). Thus our task is to construct half-lines passing through the i th AN at AoA α_i and select the particular set which gives single intersect point.

H.2.2 Ambiguity Issues

Large Scale Ambiguity

Ideally, in the absence of noise, the correct set of AoA derived at each anchor node intersects at a single point, the actual MT location (x_t, y_t) . However imperfect estimation in the presence of noise leads to deviated AoAs which intersect at three different points and form a triangle. This sometimes results in a false set of AoAs intersecting to form a smaller triangle than the correct set of AoAs at a distance very far away from actual target and hence the location error shoots up suddenly to a large value and significantly affect the performance on average. This can be better understood from the error mislocalization function with perfect radial velocities replaced by the estimated \hat{v}_i as $E = \sum_{i=1}^N (\hat{v}_i - v'_i)^2$.

As shown in Fig. 19(a) for three anchor nodes located at 1 km apart, multiple minima occur. It can be observed that the false solution occurs very far, generally lying outside the region bounded by the three ANs. Hence in order to avoid the false solutions, we constrain our region of interest only to the region formed by the set of ANs assuming that only those anchor nodes which surround the MT are considered for estimation. Another way of eliminating the false minimum is to consider the location estimate over consecutive intervals. The false minimum will change drastically while the correct estimate will be slowly varying. We need to pick the right location estimate that varies slowly thus avoiding the false minimum. This problem of multiple solutions however is not entirely solved by constraining the region alone. If the MT and any pair of ANs are collinear, then the multiple solutions may occur even for a constrained region as shown in Fig. 19(b). This can be understood intuitively that the two anchor nodes are essentially giving the same information about the MT location and not giving three different equations to solve. To tackle this problem, we

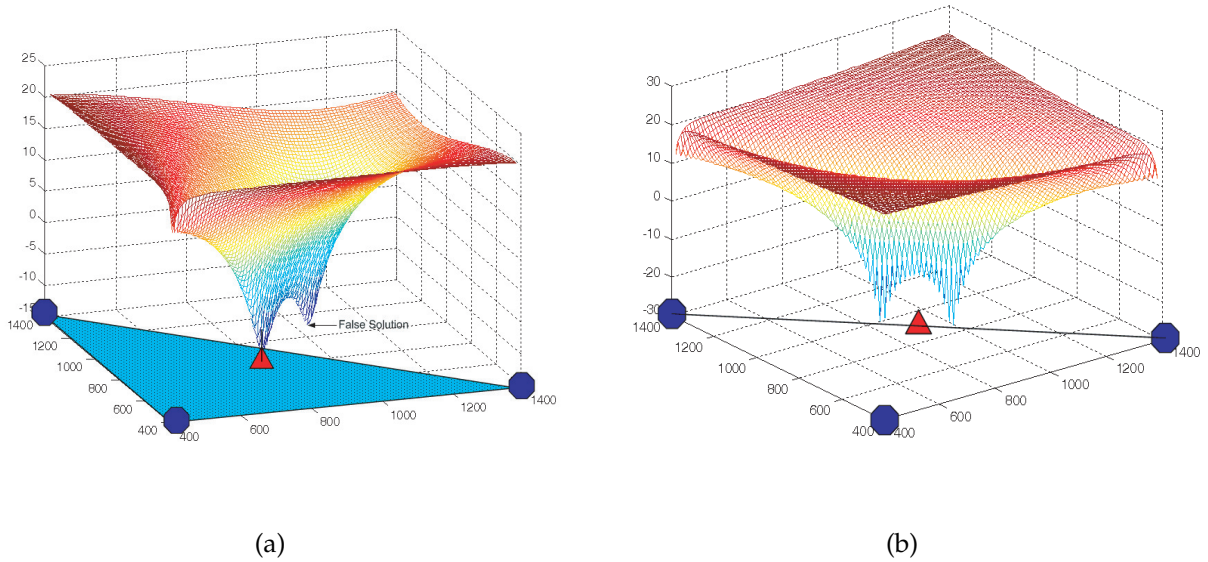


Figure 19: (a) Two peaks occur in error plot where only one corresponds to actual solution. The false solution lies outside the triangle covered by the three anchor nodes. (b) Two peaks occur in error plot even within the constrained triangle region

introduced at least one more anchor nodes which introduces more equations. Then the multiple solutions will merge to a single peak thus resolving the ambiguity.

Small Scale Ambiguity

In the presence of large noise, the centroid of the triangle formed by joining the intersection points of AoA half lines deviates too much from the actual location. Sometimes, the centroid may even fall outside the bounded region. As a remedy we introduce AoA sector scanning where we scan each AoA between the ranges $(\text{AoA}-\text{Th})$ to $(\text{AoA}+\text{Th})$ and Th is the possible error that occurs in AoA as shown in Fig. 20(a). These scanned regions of all ANs will overlap with each other. The MT resides in the region where the AoA sectors of all the ANs overlap. We then choose the centroid of this overlap region as the estimate of the location of MT. This technique ensures that the estimate lies within the bounded region and gives an estimate closest to the correct solution. To obtain the AoA error threshold Th , we plot the histogram of AoA error as shown in Fig. 20(b). If Th is too large then we are unnecessarily considering a larger overlapping region and degrading the estimation since for most of the cases error is small. On the other hand, if Th is too small then we end up

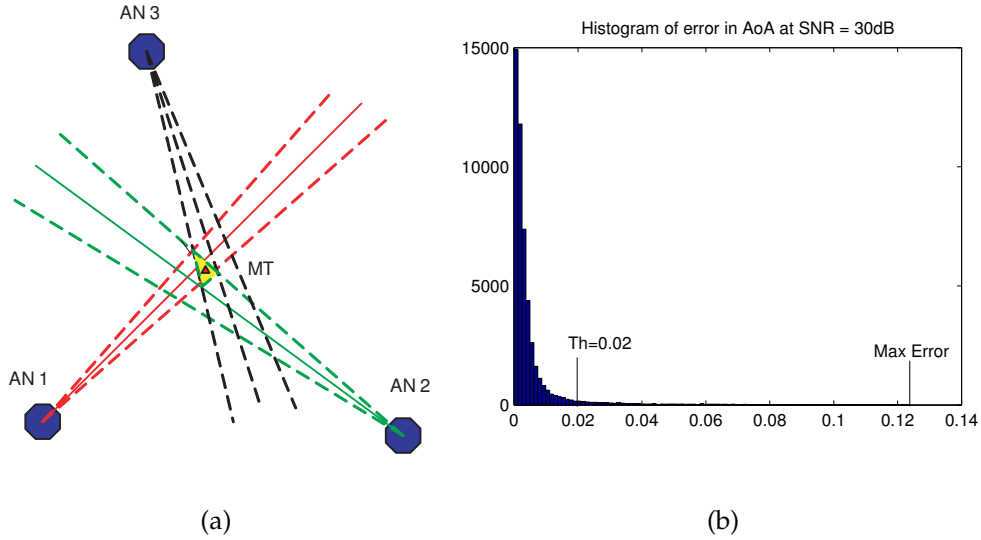


Figure 20: (a) At each AN, the region from $\text{AoA}-\text{Th}$ to $\text{AoA}+\text{Th}$ is considered and the MT location falls in the overlapping region. (b) Histogram of Error in AoA at SNR = 30dB. The threshold is chosen at the point where occurrence of error falls too low.

not having any overlap region at all in too many cases. As a tradeoff between the two extremes, we chose the threshold Th such that the number of cases with AoA error greater than Th is very small (say $\leq 2\%$) as most of the error is concentrated closer to smaller error as shown in Fig. 20(b). When the error is greater than the threshold, we average over the regions overlapped fewer times say $N - 1$, $N - 2$, $N - 3$ and so on and yet performs better than smallest triangle method. Please note that the threshold varies as per SNR value. We can clearly observe in Fig. 20(a) that this method gives smaller overlap region and closer to the actual location than the triangle formed by the intersection. Increasing anchor nodes further reduces this region of overlap and thus improving the performance. Our AoA sector scanning is a low complexity technique to determine location from imperfect AoA estimation. There are several other existing techniques that give optimum location estimate (see [9],[10],[11],[12]) that can be applied here.

H.2.3 Algorithm Flowchart

Our algorithm to estimate the location of MT for known velocity and motion direction is summarized in the flowchart shown in Fig. 21.

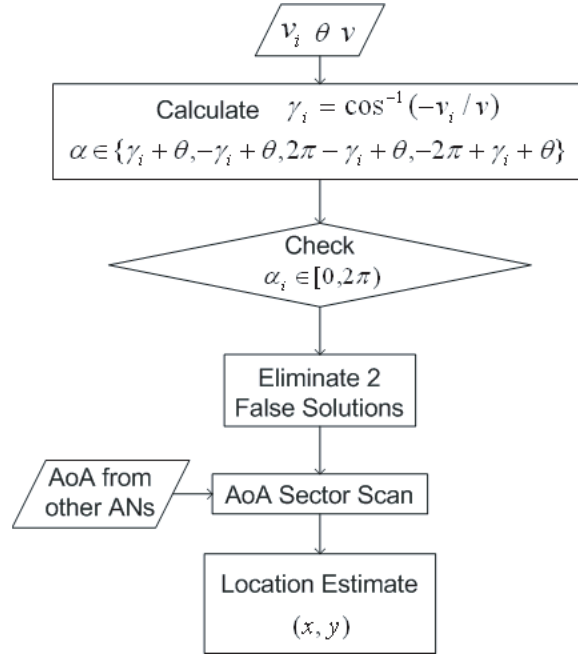
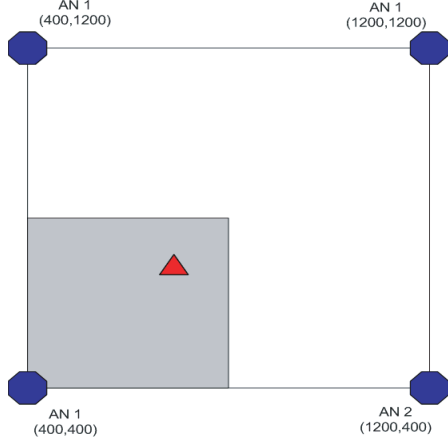


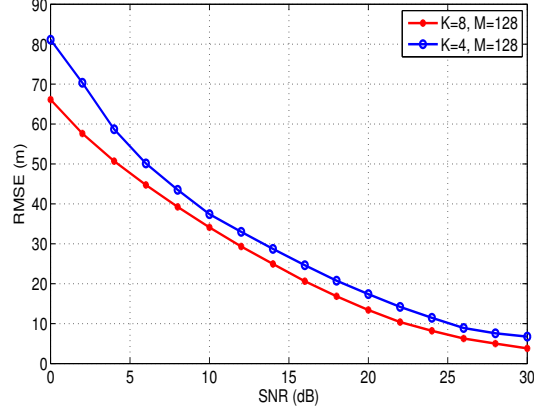
Figure 21: Flowchart of the localization technique for known v and θ of MT

H.2.4 Simulations

This section aims to analyze the performance of the algorithm and study the influence of the number of anchor nodes and temporal averaging on the performance. Simulation setup involves N anchor nodes arranged on a circle, each separated from its neighbors by a distance of 800m. Depending on the signal strength received at each anchor node, we can further constrain our region of interest thus improving accuracy. As an example, consider the setup as shown in Fig. 22(a) where there are four ANs. If the received signal strength is greater at one anchor node, then the mobile terminal is located closer to that anchor node, and we can constrain our region of interest to be the 400m x 400m square represented by shaded region. We are right now considering only LOS channel model and the velocity components are derived from the doppler shift equations. In order to suppress the noise influence on the performance, the measured velocity component is averaged M times temporally during every localization interval. With this setup and estimation method, the simulations have been done and the root mean square error (RMSE) plots have been obtained for velocity range of mobile terminal 36kmph-90kmph (10mps-25mps) for $N = 4, 8$ and $M = 128$ as shown in Fig. 22(b). We can clearly see that the performance improves as the number of anchor nodes are increased.



(a)



(b)

Figure 22: (a) Setup of 4 anchor nodes separated by 800m. MT is closer to AN 1. Hence the region of interest is constrained to the 400m x 400m shaded area. (b) RMSE vs SNR plot for known direction and velocity. Performance improves as number of anchor nodes increased and when averaged over more intervals of time

H.3 Case II: Known v , Unknown θ

For this case, the scenario is very similar to the first one except that the moving direction information of the target does not need to be measured. Since the direction θ is unknown, the method in the preceding section can not be applied here. Thus we should aim to eliminate the nuisance parameter θ and solve the nonlinear equations by relating the required quantities location coordinates (x_t, y_t) with the known quantities v , v_i , and $\{x_i, y_i\}_{i=1}^N$.

H.3.1 The Basic Algorithm

To derive the relationship between the MT location co-ordinates (x_t, y_t) and the AoA α_i , at the i th anchor node we consider the relation $\tan(\alpha_i) = \frac{y-y_i}{x-x_i}$. Let

$$\beta_i = \tan^{-1} \left(\frac{y - y_i}{x - x_i} \right) \quad (107)$$

We can easily derive the expression for α_i as

$$\alpha_i = \begin{cases} \beta_i, & \text{if } \alpha_i < \frac{\pi}{2}; \\ \pi + \beta_i, & \text{if } \frac{\pi}{2} < \alpha_i < \frac{3\pi}{2}; \\ 2\pi + \beta_i, & \text{if } \frac{3\pi}{2} < \alpha_i < 2\pi \end{cases} \quad (108)$$

Using the identity $\tan(k\pi + \omega) = \tan(\omega)$, we get

$$\tan(\alpha_i - \theta) = \tan(\beta_i - \theta) \quad (109)$$

To link known quantities v , v_i , and $\{x_i, y_i\}_{i=1}^N$ with the AoA α_i , we can re-express equation (106) as

$$1 + \tan^2(\alpha_i - \theta) = \frac{v^2}{v_i^2}$$

which implies that

$$\tan(\alpha_i - \theta) = \pm \sqrt{\frac{v^2}{v_i^2} - 1}$$

Let $\eta_i = \tan^{-1} \sqrt{\frac{v^2}{v_i^2} - 1}$ be the principal solution. Then,

$$\tan(\alpha_i - \theta) = \pm \tan(\eta_i) \quad (110)$$

Equating (109) and (110), we get

$$\tan(\beta_i - \theta) = \pm \tan(\eta_i) \quad (111)$$

In order to eliminate θ , consider the AN pair (i, j) and perform the subtraction to get

$$\tan(\beta_i - \beta_j) = \tan(\pm\eta_i \pm \eta_j). \quad (112)$$

In (112), the right hand side (RHS) can be calculated from v and v_i while for the left hand side (LHS), using the definition of β_i given in (107) and the known identity, $\tan(A - B) = \frac{\tan A - \tan B}{1 + \tan A \tan B}$, we get

$$\tan(\beta_i - \beta_j) = \left(\frac{y - y_i}{x - x_i} - \frac{y - y_j}{x - x_j} \right) / \left(1 + \frac{y - y_i}{x - x_i} \frac{y - y_j}{x - x_j} \right) \quad (113)$$

Substituting LHS and RHS back in (112) and reordering the terms, we get the equation

$$(x - A_{i,j})^2 + (y - B_{i,j})^2 = A_{i,j}^2 + B_{i,j}^2 - C_{i,j} \quad (114)$$

where

$$\begin{aligned} A_{i,j} &= \frac{x_i + x_j}{2} - \frac{y_i - y_j}{2 \tan(\pm\eta_i \pm \eta_j)} \\ B_{i,j} &= \frac{y_i + y_j}{2} - \frac{x_j - x_i}{2 \tan(\pm\eta_i \pm \eta_j)} \\ C_{i,j} &= x_i x_j + y_i y_j + \frac{x_i y_j - x_j y_i}{\tan(\pm\eta_i \pm \eta_j)} \end{aligned}$$

The RHS in (114) on simplification gives

$$A_{i,j}^2 + B_{i,j}^2 - C_{i,j} = \frac{d_{i,j}^2}{4} \left(1 + \frac{1}{\tan^2(\pm\eta_i \pm \eta_j)} \right) > 0 \quad (115)$$

where $d_{i,j}$ is the distance between the AN i and AN j . Thus (114) is of the form of equation of a circle with center co-ordinates as $(A_{i,j}, B_{i,j})$ and radius as

$$r = \sqrt{A_{i,j}^2 + B_{i,j}^2 - C_{i,j}} = \frac{d_{i,j}}{2} \sqrt{1 + \frac{1}{\tan^2(\pm\eta_i \pm \eta_j)}}.$$

Interestingly, these circles have the following properties:

- The circle corresponding to the AN pair (i, j) , $(x - A_{i,j})^2 + (y - B_{i,j})^2 = A_{i,j}^2 + B_{i,j}^2 - C_{i,j}$ passes through ANs i and j . This can be verified easily by substituting the AN's co-ordinates in the equation.
- For N ANs we get $(N - 1)$ independent circles for each of 2^N different combinations of $\pm\eta_i$ of which only one particular combination of $(N - 1)$ circles intersect at a single point (other than at AN itself) which is the MT location.

H.3.2 Ambiguity Issues

Similar to the known velocity (v) and known direction (θ) case, ambiguity issues arise in this unknown direction case due to imperfect estimation of radial velocities at the ANs. The large scale ambiguity is combated by constraining the region to the area bounded by ANs and by increasing the number of ANs. The small scale ambiguity is combatted in similar way as AoA sector scanning, except that instead of AoA we have the quantity $P_{i,j} = \tan(\pm\eta_i \pm \eta_j)$ and we plot error histogram from $P_{i,j}$ and sweep it between $(P_{i,j} \pm Th)$ for each circle and determine the overlap region. The centroid of this overlapping region is taken as the location estimate.

H.3.3 Algorithm Flowchart

Our algorithm to estimate location of MT for known velocity and unknown direction is summarized in the form of flowchart shown in Fig. 23.

H.3.4 Simulations

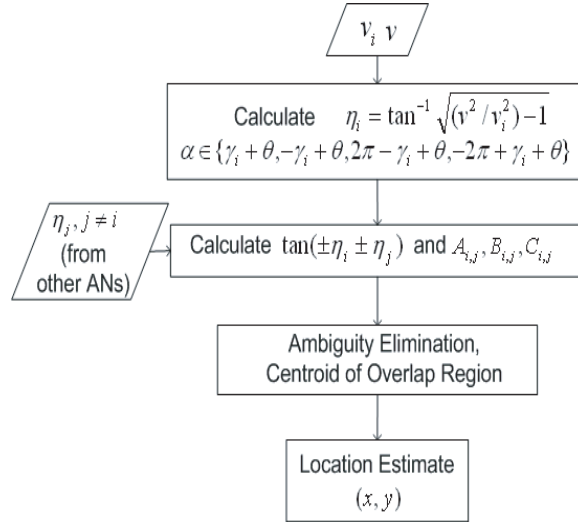


Figure 23: Flowchart of the localization technique for known v and unknown θ of MT

The simulation setup is exactly same as the known direction case as explained in detail earlier. The performance plot is as shown in the Fig. 24. The performance of our technique for the unknown direction case is similar to that of the known direction case but this is obtained at the cost of increased computation and minimum number of ANs required.

H.4 Summary

We presented a new approach to find the location of a moving target using the observed radial velocities from Doppler. We specifically focused on two cases - 1) Velocity (v) and direction of motion (θ) of the moving target are known 2) Only velocity (v) is known and direction (θ) is unknown. We provided methods to estimate location coordinates of the moving target by solving a set of nonlinear equations. Our approach imposes no requirement of common time base between any two nodes and avoids large expensive antenna arrays at the anchor nodes. Since our technique benefits from the motion of the target, the performance improves as the mobility increases.

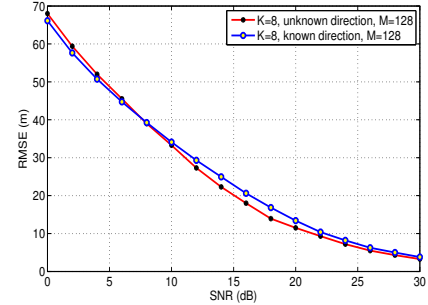


Figure 24: RMSE vs SNR plot for the unknown direction and known velocity. Performance improves as number of anchor nodes increased. The performance for known and unknown direction cases is similar

I Publications

1. M. Ouertani, H. Xu, L. Yang, , and H. Besbes, "Differential (de-)modulation for orthogonal bi-pulse noncoherent UWB," in *Proc. of International Conf. on Communications*, Dresden, Germany, June 14–18, 2009.
2. N. Wang and L. Yang, "A semidefinite programming approach for cooperative localization," in *Proc. of Asilomar Conf. on Signals, Systems, and Computers*, Pacific Grove, CA, November 7–10, 2010.
3. N. Wang and L. Yang, "Further results on cooperative localization via semidefinite programming," in *Proc. of Conf. on Info. Sciences and Systems*, Baltimore, MD, March 23–25, 2011.
4. N. Wang and L. Yang, "Semidefinite programming for GPS," in *24th International Technical Meeting of the Satellite Division of the Institute of Navigation (ION GNSS 2011)*, Portland, OR, September 19–23, 2011.
5. H. Xu and L. Yang, "Calibration of random phase rotation for multi-band ofdm uwb signals," in *Proc. of Asilomar Conf. on Signals, Systems, and Computers*, Pacific Grove, CA, November 7-10, 2010.
6. H. Xu and L. Yang, "ToA estimation for MB-OFDM UWB by suppressing energy leakage," in *Proc. of MILCOM Conf.*, San Jose, CA, October 31–November 3, 2010.
7. H. Xu, L. Yang, and C.-C. Chong, "Low-complexity receivers for multi-carrier pulse position modulation," in *Proc. of Vehicular Technology Conf.*, Taipei, Taiwan, May 2010.
8. H. Xu, L. Yang, Y. T. J. Morton, and M. M. Miller, "Mistiming performance analysis of the energy detection based ToA estimator for MB-OFDM," *IEEE Trans. on Wireless Communications*, vol. 8, no. 8, pp. 3980–3984, August 2009.
9. H. Xu, W. Zhang, and L. Yang, "Wireless localization and ranging with ultra-wideband signals," in *Proc. of Intl. Conf. on Ultra-Wideband*, Bologna, Italy, September 14–16, 2011.
10. L. Yang and H. Xu, "Ultra-wideband localization," in *Position Location - Theory, Practice and Advances: A Handbook for Engineers and Academics*, S. Zekavat and M. Buehrer, Eds. Wiley, 2011.

11. W. Zang, W. Zhang, and L. Yang, "On the optimality of timing with dirty templates," in *Proc. of Global Telecommunications Conf.*, Honolulu, Hawaii, November 30–December 4, 2009.
12. W. Zhang and L. Yang, "Delay-doppler span estimation in OFDM radar," in *Proc. of Conf. on Info. Sciences and Systems*, Baltimore, MD, March 23–25, 2011.
13. W. Zhang, L. Yang, and W. Zang, "On the optimality of timing with dirty templates," *IEEE Trans. on Communications*, 2012.